DEVELOPMENT OF HOLE TRANSPORT TRANSPARENT CONDUCTIVE ELECTRODES FOR N-TYPE CRYSTALLINE SILICON SOLAR CELLS

A THESIS SUBMITTED TO
THE GRADUATE SCHOOL OF NATURAL AND APPLIED SCIENCES
OF
MIDDLE EAST TECHNICAL UNIVERSITY

BY

OZAN AKDEMİR

IN PARTIAL FULFILLMENT OF THE REQUIREMENTS
FOR
THE DEGREE OF MASTER OF SCIENCE
IN
MICRO AND NANOTECHNOLOGY

DECEMBER 2018

Approval of the thesis:

DEVELOPMENT OF HOLE TRANSPORT TRANSPARENT CONDUCTIVE ELECTRODES FOR N-TYPE CRYSTALLINE SILICON SOLAR CELLS

submitted by **OZAN AKDEMİR** in partial fulfillment of the requirements for the degree of **Master of Science in Micro and Nanotechnology Department, Middle East Technical University** by,

Prof. Dr. Halil Kalıpçılar
Dean, Graduate School of **Natural and Applied Sciences** _____

Prof. Dr. Burcu Akata Kurç
Head of Department, **Micro and Nanotechnology** _____

Assoc. Prof. Dr. Alpan Bek
Supervisor, **Micro and Nanotechnology, METU** _____

Assist. Prof. Dr. Bilge İmer
Co-Supervisor, **Metallurgical and Materials Eng., METU** _____

Examining Committee Members:

Assoc. Prof. Dr. Mehmet Emre Taşgın
Institute of Nuclear Sciences, Hacettepe University _____

Assoc. Prof. Dr. Alpan Bek
Micro and Nanotechnology, METU _____

Prof. Dr. Hüsnü Emrah Ünalan
Metallurgical and Materials Engineering, METU _____

Assoc. Prof. Dr. Emren Nalbant Esentürk
Chemistry, METU _____

Assist. Prof. Dr. Bilge İmer
Metallurgical and Materials Engineering, METU _____

Date: 27.12.2018

I hereby declare that all information in this document has been obtained and presented in accordance with academic rules and ethical conduct. I also declare that, as required by these rules and conduct, I have fully cited and referenced all material and results that are not original to this work.

Name, Surname: Ozan Akdemir

Signature:

ABSTRACT

DEVELOPMENT OF HOLE TRANSPORT TRANSPARENT CONDUCTIVE ELECTRODES FOR N-TYPE CRYSTALLINE SILICON SOLAR CELLS

Akdemir, Ozan
Master of Science, Micro and Nanotechnology
Supervisor: Assoc. Prof. Dr. Alpan Bek
Co-Supervisor: Assist. Prof. Dr. Bilge İmer

December 2018, 71 pages

Conventional transparent conductive electrodes (TCEs) used in crystal silicon (c-Si) solar cells are commonly made of indium tin oxide (ITO) which provides low sheet resistance and high transparency. However, due to indium scarcity, ITO layers increase the fabrication cost; thus, alternative TCEs, such as fluorine-doped tin oxide (FTO), zinc oxide (ZnO), metal nanowires and Oxide/Metal/Oxide (OMO) multilayers, are being investigated. Conventional solar cells also make use of doped layers, to create the junction and back surface field that leads to several intrinsic losses such as parasitic absorption and doping related recombination. Dopant-free carrier selective contacts, that enable one type of carrier to pass while blocking the other type, are being studied as replacements of doped layers in c-Si solar cells. In this study, OMO multilayers with molybdenum oxide (MoO_x), and silver (Ag) are formed via thermal evaporation as dopant-free hole transport transparent conductive electrodes (HTTCEs) for n-type c-Si solar cells. Semi-dopant-free c-Si cells, made from wafers with different doping concentrations that utilize OMO multilayers are compared in terms of solar cell performance. Comparison of two HTTCE design, optimizations of outer MoO_x layer thickness and Ag deposition rates, and comparison of pyramid textured and flat surface solar cells are performed to increase optical and electrical

properties. An efficiency of 9.3 ± 0.2 % is achieved with a pyramid textured semi-dopant-free solar cell that employs HTTCE structure. Results of this study can be used in research on dopant-free solar cells and any other photonic applications that require TCE layers.

Keywords: Transparent Conductive Electrode, Dopant-free Solar Cell, Carrier Selective Contact, Molybdenum Oxide

ÖZ

N-TİPİ KRİSTAL SİLİSYUM GÜNEŞ GÖZELERİ İÇİN DEŞİK SEÇİCİ İLETKEN SAYDAM ELEKTROT ÜRETİLMESİ

Akdemir, Ozan
Yüksek Lisans, Mikro ve Nanoteknoloji
Tez Danışmanı: Doç. Dr. Alpan Bek
Ortak Tez Danışmanı: Dr. Öğr. Üyesi Bilge İmer

Aralık 2018, 71 sayfa

Kristal silisyum güneş gözelerinde kullanılan geleneksel İletken Saydam Elektrotlar (İSE), düşük tabaka direnci ve yüksek ışık geçirgenliği elde etmek için İndiyum Kalay Oksit'ten (ITO) üretilirler. İndiyum kaynaklarının az olması sebebi ile, ITO tabakaları güneş gözelerinin üretim maliyetlerini arttırır. Bu sebeple; Flor katkılı Kalay Oksit (FTO), Çinko Oksit (ZnO), metal nanoteller ve Oksit/Metal/Oksit (OMO) tabakaları gibi ITO'ya alternatif İSEler araştırılmaktadır. Geleneksel kristal silisyum güneş gözelerinde eklem ve arka yüzey alanı yaratmak için kullanılan katkılanmış katmanlar, parazit ışık soğurulması ve katkılama kaynaklı yük taşıyıcı birleşmesi gibi kayıplara sebep olur. Katkılanmış katmanların yerine kullanılmak için, bir tip taşıyıcıyı geçirirken diğer tip taşıyıcının geçmesini engelleyen katkısız taşıyıcı seçici kontaklar araştırılmaktadır. Bu çalışmada termal buharlaştırma yöntemi kullanılarak, molibden oksit (MoO_x) ve gümüş (Ag) malzemelerinden oluşan OMO katmanları, kristal silisyum güneş gözeleri için deşik seçici iletken saydam elektrot (DSİSE) tabakası olarak kullanılmak üzere üretildi. DSİSE farklı katkılama konsantrasyonuna sahip yarı-katkısız kristal silisyum alt taşlardan üretilmiş güneş gözelerinin performansları karşılaştırıldı. Optik ve elektrik özelliklerinin iyileştirilmesi için Ag kaplama hızı ve dıştaki MoO_x katman kalınlıklığının optimizasyonu, iki farklı DSİSE

modelinin karşılaştırması ve piramit yapılı yüzeyli ve düz yüzeyli güneş gözelerinin karşılaştırması yapıldı. Piramit yapılı yarı-katkısız bir güneş gözesinden %9.3±0.2'lik verim elde edildi. Bu çalışmanın sonuçları özellikle katkısız güneş gözesi araştırmalarında ve İSE yapısı içeren diğer fotonik uygulamalarda kullanılabilir.

Anahtar Kelimeler: İletken Saydam Elektrot, Katkısız Güneş Gözesi, Taşıyıcı Seçici Kontak, Molibden Oksit

To my beloved family..

ACKNOWLEDGMENTS

First of all, I would like to express my gratitude to my advisor Assoc. Prof. Dr. Alpan Bek, for his support, positive attitude and guidance throughout my undergraduate and M.Sc. education. His extensive knowledge and counseling have been a tremendous help in my studies.

I would like to thank Prof. Dr. Raşit Turan for giving me the opportunity to work in GÜNAM laboratories and for his experienced advices, about both academic and daily life.

I'm extremely grateful to Dr. Hisham Nasser for his invaluable mentoring and Mona Zolfaghari Borra for her endless help even in her busiest times. The completion of my thesis would not have been possible without their support and friendship.

I would like to extend my sincere thanks to Ezgi Genç for being a great study partner, Gamze Kökbudak for her joyful friendship, Efe Orhan for his brotherly attitude, Dr. Fırat Es and Emel Semiz for their positive encouragements, and Alp Ege Aytaç and Baran Utku Tekin for their support and friendship since undergraduate years.

I would also like to thank all researchers and staff in GÜNAM and Nano-Optics group; especially to İbrahim Murat Öztürk, Özge Demirtaş, Buket Gökbakan, Gülsen Baytemir and Emine Hande Çiftpınar for their help and support.

I kindly acknowledge financial support from TÜBİTAK under project no: 113M931 and 115M061.

My deepest gratitude goes to Sevgi Ericek for giving me endless support and motivation, regardless of the physical distance between us.

Last but not least, I would like to thank my family for the love and support they gave and continue to give me in every step of my life.

TABLE OF CONTENTS

LIST OF TABLES

TABLES

LIST OF FIGURES

FIGURES

CHAPTER 1

INTRODUCTION

In this study, hole transport transparent conductive electrode (HTTCE) multilayers that acts as both transparent conductive electrode (TCE) and hole selective contacts for n-type crystal silicon (c-Si) solar cells are developed via thermally evaporated molybdenum oxide (MoO_x) and silver (Ag) thin films. The HTTCE multilayers are developed to overcome some problems in conventional c-Si solar cells that utilize indium tin oxide (ITO) layers as TCE's, and highly doped layers to create junction and back surface field (BSF). A power conversion efficiency of 9.3 ± 0.2 % is achieved from a semi-dopant-free solar cell that employs HTTCE front contact.

In order to compete with fossil fuels as the primary energy source, decreasing the fabrication cost of solar cells is one of the main focuses of photovoltaics (PV) community. Although the most expensive part of conventional solar cell fabrication is the fabrication of c-Si base [Glunz et al., 2012], cost-reduction while preserving high efficiencies by using cheaper materials in other parts of the devices is still a necessity. Due to scarcity of indium on earth, ITO layers increase the fabrication cost of solar cells, and alternative TCEs that does not employ ITO layers are being investigated.

Another focus of the PV community is to increase the power conversion efficiency by reducing the optical and electronical losses within solar cells. Although it is widely utilized in conventional solar cells to create junction and BSF, doping increases intrinsic losses such as parasitic absorption and auger recombination in the device. In addition, it is a high temperature process that includes toxic materials; thus, it increases the fabrication cost of devices. For such reasons, dopant-free carrier selective contacts that has simple deposition techniques are being researched to

fabricate dopant-free solar cells, for which above 20% efficiencies have already been demonstrated [Bullock et al., 2018].

In this work, HTTCE multilayers are designed as Oxide/Metal/Oxide multilayers that acts as TCE's while also working as a hole selective contact due to the MoO_x/c-Si contact. In Chapter 2, a brief overview of photovoltaics and detailed explanations of TCEs and carrier-selective contacts are presented. The chapter also includes a section that describes the hole selectivity of MoOx and another section that gives examples of dopant-free solar cell studies.

The experimental methods and fabrication of semi-dopant-free solar cells that employs HTTCE structures as hole selective front contact and n+ doped layer as rear contact, are described in detail in Chapter 3.

In Chapter 4, comparison of five different c-Si wafers, comparison of two different HTTCE designs, effect of deposition rates for Ag layers, comparison of textured and polished c-Si substrates, and effect of outer MoO_x layer thickness on optical and electronical properties of HTTCE are reported. A power conversion efficiency of 9.3 ± 0.2 % is achieved from a semi-dopant-free solar cell that employs MoOx/Ag/MoO_x HTTCE on pyramid textured c-Si, without any passivation layers between c-Si and contacts.

CHAPTER 2

THEORY

2.1. Photovoltaics

The process of converting sunlight into electricity via solar cells, which are usually made of semiconductors, is called photovoltaics (PV). The first solar cell was reported in 1941 [Ohl, 1941], followed by major improvements in efficiencies in 1950s [Glunz et al., 2012] and the PV industry have grown rapidly ever since, especially in recent years due to increasing concerns on global warming and greenhouse gas emissions that are stimulated by conventional energy sources like fossil fuels. A brief overview of physics behind PV is given in this section, to have a better understanding of the solar cell operation.

2.1.1. Band Gap

It is known from main principles of quantum mechanics that the energy of a system is quantized; thus, electrons in a free atom can only occupy certain energy levels and two electrons at most can be present in an energy level, one being spin-up and the other one being spin-down, according to the Pauli exclusion principle. Therefore, when two atoms come together to form a molecule, as the distance between them decrease, the energy levels split into two, one higher (antibonding) and one lower (bonding) levels, due to interactions of electrons and nuclei of the two atoms. At an equilibrium distance between atoms, the bonding level is at the lowest energy configuration, and further decrease of the atomic separation results in increase of energy of the bonding level, due to Coulomb repulsion forces between nuclei of atoms.

In a macroscopic solid material, where many atoms come together, the splitting of many levels results in formation of energy bands. At absolute zero temperature, for non-metals, valence band is the highest band occupied by electrons

and conduction band, which is above valence band, is the lowest band that has vacant states for electrons. In between these bands, there is a forbidden gap where energy states can not exist, and this gap is called the band gap (E_g). E_g is an important property, which determines the conductivity and absorption of the materials. Insulator materials have large E_g while semiconductors have smaller E_g. Conductors either have a very small band gap or their valence and conduction bands overlap, and they don't have an E_g. [Quimby, 2006]

2.1.2. Semiconductor Materials

Semiconductor properties can be found in materials from group IV elements in the periodic table, or in combination of elements in group III and V or group II and VI elements; which are called III-V semiconductors and II-VI semiconductors, respectively. Semiconductors have different electrical and optical properties based on the elements they are composed of, and silicon (Si) is the most common semiconductor material that is used in various applications in the industry, from integrated circuit chips to solar cells. Electrical properties of semiconductors can be altered by doping them with impurity atoms to increase the concentration of one type of charge carrier; either electrons or holes. Atoms that increase the electron concentration are called donors and they make the material n-type, while atoms that increase the concentration of holes; which are the absence of electrons that act as positive charges, makes the material p-type, and they are called acceptors.

An important property to consider when dealing with semiconductors is the Fermi level (E_F), which is defined as the energy level that at absolute zero temperature (0 Kelvin), no electron can be occupied in the energy states above it. It is equal to the electrochemical potential of electrons at 0 Kelvin and can be explained by the Fermi-Dirac distribution function given in Eq. 2.1 below, where μ is the chemical potential, k_B is the Boltzmann constant and T is the absolute temperature. Eq. 2.1 gives the probability of electron occupation of a state with energy E. At absolute zero, occupation probability of states with E below E_F is 1, while the ones with E above E_F is zero. [Kittel,2005]

$$f(E) = \frac{1}{1+e^{\frac{E-\mu}{k_B T}}} \tag{2.1}$$

For an intrinsic semiconductor, which is not introduced to any impurity doping, the E_F lies exactly in the middle of E_g. However, for an n-type semiconductor E_F is just below the conduction band and for a p-type semiconductor, it is just above the valence band.

2.1.3. Absorption of Light

When a photon is incident on a semiconductor, if the photons energy (hν) is smaller than E_g, the material is transparent to the photon with that wavelength. If hν is equal to or greater than the E_g of the material, the material absorbs the photon. Absorbed energy excites an electron from the conduction band to the valence band, leaving a hole in the valence band, thus, generating charge carriers.

$$\alpha = \frac{4\pi k}{\lambda} \tag{2.2}$$

Depending on its wavelength, incident light can penetrate into the semiconductor before being absorbed. Absorption coefficient (α), which varies for different materials, is used to determine this penetration of light. Eq. 2.2 represents α, where λ is the wavelength of incident light and *k* is the extinction coefficient; which is the imaginary part of complex refractive index and it determines the rate of absorption of light in the material [Pedrotti et al., 1992]. Absorption depth of light with certain wavelength is defined by the inverse of α; thus, high energy photons (short wavelength) are expected to be absorbed closer to the surface while low energy photons (long wavelength) can penetrate deeper into the material before being absorbed.

2.1.4. Generation Rate of Charge Carriers

As mentioned in the previous section, charge carriers are generated by the absorption of light. The amount of light absorption depends on α, as well as the thickness of the material. Intensity of light at any depth inside the material can be

calculated from Eq. 2.3, where I_0 is the intensity of light on the surface and x is the depth into the material for which the intensity is being calculated. Keep in mind that the reflection from the surface is neglected from this equation.

$$I = I_0 e^{-\alpha x} \tag{2.3}$$

Charge carrier generation rate (G), which is the number of carriers generated at a point in the material via absorption of light, can be found by assuming the intensity loss is directly related to charge carrier generation. Differentiating Eq. 2.3 gives the change in light intensity; thus, it gives the generation of carriers at any point in the material. Hence, G can be calculated by Eq. 2.4, where N_0 is the photon flux at the surface. Equations 2.3 and 2.4 show that light intensity decreases exponentially deeper into the material; thus, G is higher in points closer to the surface, than deeper points.

$$G = \alpha N_0 e^{-\alpha x} \tag{2.4}$$

2.1.5. Recombination

When an electron in the valence band is excited to the conduction band via absorption of a photon, it is actually transferred to a meta-stable state. Hence, after some time, it returns to the valence band and recombines with the hole that is generated with the excitation of electron. The average time between the generation and recombination of an electron-hole pair is called lifetime, and longer lifetime materials are preferred for solar cells, since they result in better efficiencies. In a solar cell operation, recombination losses hinder the performance of the devices; therefore, it is important to understand the recombination mechanisms and design the solar cells accordingly. Radiative, Auger and Shockley-Read Hall (SRH) are the three types of recombination.

Radiative recombination, which is represented in Figure 2.1, is the direct recombination of electron in the conduction band with hole in the valence band, which results with emission of a photon which has an energy similar to E_g, so it is only weakly absorbed and leaves the semiconductor material.

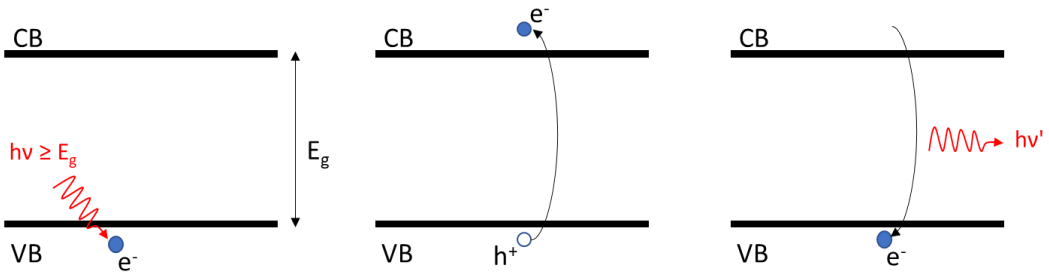

Figure 2.1. Representation of radiative recombination

Auger recombination, on the other hand, does not result in emission of a photon. Instead of releasing its energy as a photon, the recombining electron transfers its energy to another electron in the conduction band and excites it to a higher energy level within the same band. The newly excited electron then, releases its energy as a phonon and relaxes back down to the edge of the conduction band.

SRH is a recombination mechanism that is related to the defects in the semiconductor material; thus, it is not present in perfectly pure materials that has no defects. This recombination mechanism occurs due to trap state formation in the band gap, caused by defects that are either unintentionally or intentionally formed in the material. If one type of carrier is trapped in this state and an opposite type carrier also moves to this band, before the first one moves on to another, recombination occurs.

Either inside or at the surface of the semiconductor, defects promote recombination. Since the surface can be considered as a disruption of the crystal lattice and has dangling bonds, recombination is very high there. Passivation layers are used in solar cells to fill the dangling bonds and reduce recombination.

2.1.6. Carrier Transport

Electrons and holes are considered as free carriers, when they are in conduction and valence band, respectively. These free carriers move randomly to random directions in the crystal lattice and changes direction after scattering from the atoms in the lattice. Unless there is a concentration gradient, that induces diffusion, or an electric field, that causes drift motion, free carriers are considered to have no net motion.

Diffusion occurs when the carrier concentration in a region is higher than other regions. In such a case, the random movement of free carriers have a net direction towards low concentration areas from the higher concentration regions. Eventually the concentration becomes similar in every region and the carriers again move randomly with no net motion.

When the semiconductor is under the influence of an electric field, electrons tend to move in a net direction opposite to the direction of the electric field, while holes move in a net direction that is the same direction of the electric field. This is called the drift motion of charge carriers. Diffusion and drift are the main transport mechanisms of charge carriers in semiconductors.

2.1.7. P-n Junction

P-n junctions are formed by contacting a p-type and an n-type semiconductor. After the initiation of contact, due to diffusion, electrons from n-type tend to move to the p-type and holes from p-type move to the n-type. This aligns the fermi levels of the semiconductors and when the equilibrium is reached, a region in the vicinity of the junction, that has no free charge carriers within, is formed. This region is called space charge region (SCR). While reaching the equilibrium, the diffusion of charge carriers creates fixed charged ions on the junction edges of p-type and n-type semiconductors. Diffusion of holes to the n-type, leaves negatively ionized acceptors on p side while diffusion of electrons to the p-type leaves positively ionized donors on the n side. This creates an internal electric field (E-field) in the SCR and curves the bands of semiconductors that, in equilibrium, forms energy barriers for electrons in the conduction band of n-type and for holes in the valence band of p-type semiconductor. Any charge carriers that are formed in the SCR is therefore, drawn into their respective sides, that is the holes move to p side while electrons move to n side, via drift motion due to the electric field in the region [Omnes, 2010]. The p-n junction and movement of carriers are illustrated in Figure 2.2.

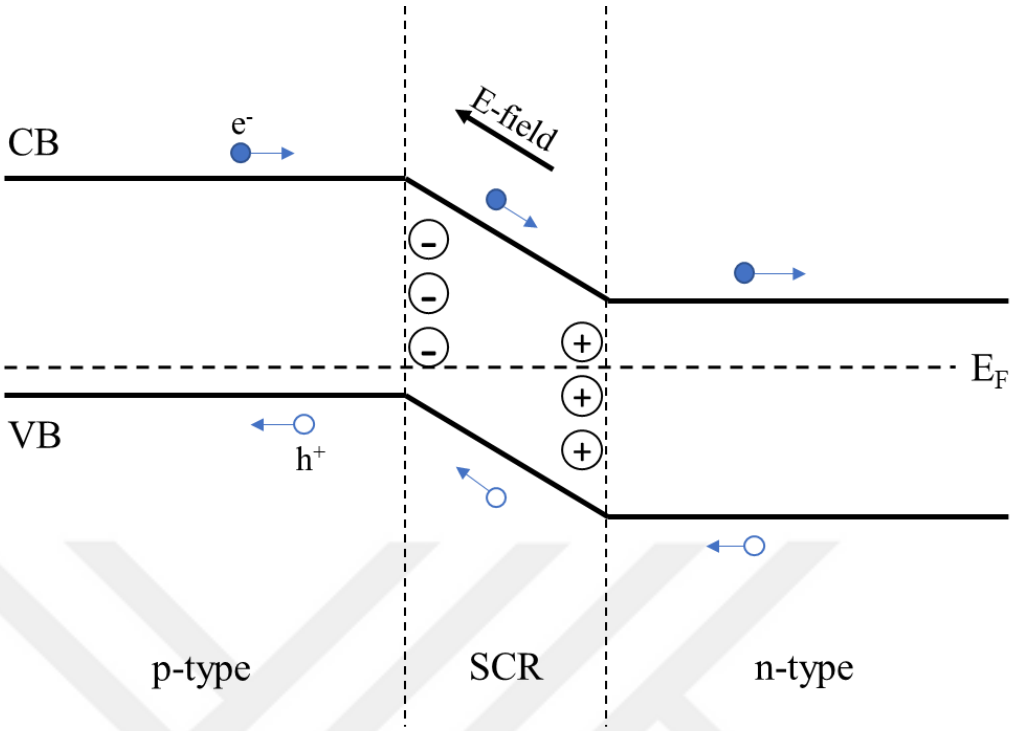

Figure 2.2 Illustration of a p-n junction

2.1.8. Solar Cells

As mentioned in the first section of this chapter, solar cells are devices that convert sunlight into electricity. Solar cells work on four basic principles; absorption of light, generation, transportation and collection of charge carriers. Light incident on the cell is absorbed and generates an electron-hole pair. The generated carriers move towards their respective contacts and collected there to provide current to an external circuit. When an electron-hole pair is generated by light absorption, they recombine after a time equal to the minority carrier lifetime, if they are not collected. Carriers can be collected before this recombination can take place in p-n junctions due to the electric field in the junction that sends the minority carrier to the region where it is a majority carrier; therefore, materials with such structure are commonly used in solar cells. In order to be affected by this electric field, minority carrier must reach the SCR first; so, the collection probability is higher for carriers that are generated close to the SCR, which is an important fact for design configurations.

2.2. Photovoltaic Characteristics

There are certain characteristics that imply the performance of solar cells. In this section, those characteristics are briefly explained.

2.2.1. Quantum Efficiency

Quantum efficiency is the ratio of the number of collected carriers to the number of photons (of certain wavelengths) incident on the solar cell. If every carrier generated by photons with a certain wavelength is collected, than the quantum efficiency for that wavelength is unity; however, usually that is not the case, due to optical losses and recombinations during carrier transport. There are two types of quantum efficiency; external and internal. External quantum efficiency (EQE) is the ratio of the number of collected carriers directly to the number of photons incident on the solar cell, while internal quantum efficiency (IQE) is the ratio of the number of collected carriers to the number of photons that generate the carriers; that is the number of photons that are absorbed and not lost due to reflection or transmission.

An EQE analysis gives an idea about optical and recombinational losses in solar cells, which can be interpreted by observing the difference of measured quantum efficiency to the ideal unity case. IQE can be calculated by correcting the EQE measurement with reflectance and transmission measurements, to have a better understanding of the recombinational losses of the device.

2.2.2. I-V Curve

In solar cells, I-V curve depends on the electrical behaviours of solar cell diode in both dark and illuminated conditions. It is represented with the solar cell diode equation, given as Eq. 2.5, where n is the ideality factor, k is the Boltzmann constant, T is absolute temperature in Kelvin, q is the elementary charge, I_L is the light generated current and I_0 is the dark saturation current. I_0 represents the recombination in the device, higher I_0 means high recombination. Representation of an I-V curve of a solar cell close to ideal conditions is given in Figure 2.3.

$$I = I_L - I_0(e^{\frac{qV}{nkT}} - 1) \quad (2.5)$$

From an I-V curve; open circuit voltage (V_{oc}), short circuit current (I_{sc}), fill factor (FF) and power conversion efficiency (η), which are important parameters that indicates the performance of the solar cells, can be extracted. In addition, current density vs voltage (J-V) curves are commonly used instead of I-V curves to cancel the effect of area of the cells, where J is the current divided by the area of the cell.

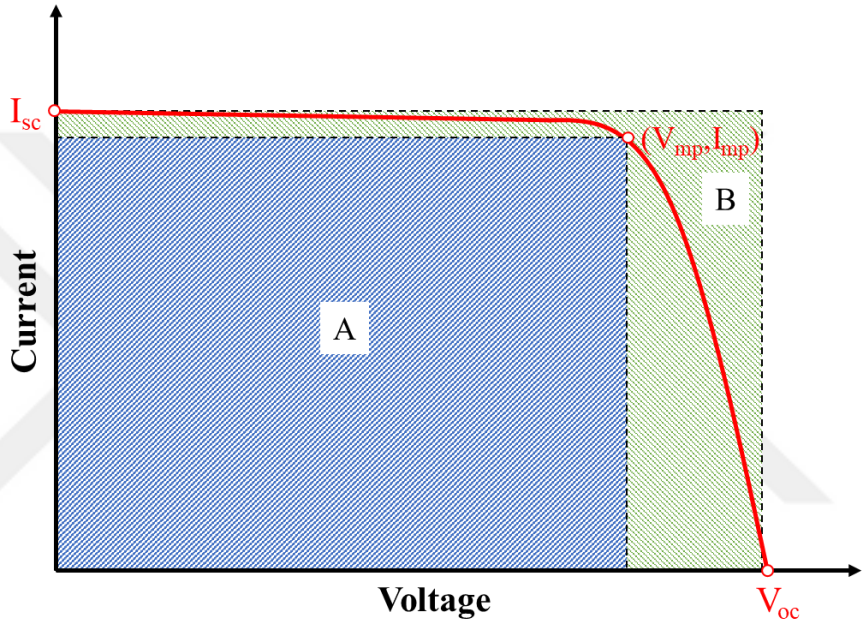

Figure 2.3 I-V curve example

2.2.3. Short Circuit Current

I_{sc} is the maximum current of the solar cell, when the voltage across the device is zero, which is marked in Figure 2.3. Short circuit current density (J_{sc}), which is basically the I_{sc} divided by the area of the solar cell, is more commonly used to characterize the performance of the solar cells. Generation and collection of charge carriers are the main factors that affect J_{sc}. Therefore, absorption and reflection of the solar cells, which determine the amount of incident light on solar cell that generates charge carriers, and surface passivation and minority carrier lifetime that determine the collection probability of charge carriers are important parameters for J_{sc}.

2.2.4. Open Circuit Voltage

V_{oc} is the maximum voltage of the solar cell, when the current through the device is zero. It is represented in Eq. 2.6. Since the variation in I_L is usually very small, V_{oc} mainly depends on I_0, which can have variations by orders of magnitude. Since the recombination of charge carriers is the defining factor for I_0, it is also the most significant mechanism in the solar cell operation that affects V_{oc}.

$$V_{oc} = \frac{nkT}{q} \ln\left(\frac{I_L}{I_0} + 1\right) \tag{2.6}$$

2.2.5. Fill Factor

FF is a parameter that gives an idea about the power of the solar cell and the resistive losses. It is represented in Eq. 2.7, where V_{mp} and I_{mp} are the voltage and current values, respectively, at the maximum power of solar cell. FF can also be described as area A divided by area B in Figure 2.3, thus, it is also referred as "the squareness of the I-V curve".

$$FF = \frac{V_{mp} \times I_{mp}}{V_{oc} \times I_{sc}} \tag{2.7}$$

2.2.6. Power Conversion Efficiency

Power conversion efficiency (η) is the main parameter that is used to compare the performance of solar cells. As its name suggests, it represents how efficient the solar cell is converting incident power to electricity. Generally, Eq. 2.8 is used for calculating η, where P_{in} is the power of sun light incident on the solar cell.

$$\eta = \frac{V_{oc} \times I_{sc} \times FF}{P_{in}} \tag{2.8}$$

2.2.7. Series and Shunt Resistance

Series and shunt resistances are parasitic resistance effects that affect the efficiency of solar cells, mainly by determining FF of the devices. Series resistance occurs in solar cells due to the resistance between emitter and base of the solar cell, the contact resistance of metal and Si, and the resistance of the top and rear metal

contacts; therefore, the design of the solar cell is a very important factor for series resistance. Increase in series resistance result in decrease of FF and thus, decreases η. Shunt resistance, on the other hand, needs to be high, to get better efficiencies, since low shunt resistance means that photocurrent is finding alternative paths in the material and does not contribute to power output of the device. Shunt resistance is typically related to material defects caused by flaws in manufacturing. Existance of both of these resistance effects can be interpreted by analysing the I-V curve of a solar cell, since they have certain affects on the squareness of the curve.

2.3. Crystal Silicon Solar Cells

Solar cells based on various materials have been developed throughout the years, such as dye-sensitized solar cells, cadmium telluride (CdTe) solar cells and copper indium gallium selenide (CIGS) solar cells [Goetzberger et al., 2003]; however, c-Si is still the dominant material used in conventional PV devices, as it was accounted for about 95% of all production in PV market globally in 2017 [©Fraunhofer ISE, 2018]. C-Si owns this sovereignty to several facts, such as its early realization as a material for solar cell production and parallel development with microelectronic industry, as well as its exceptional properties, specifically it being a non-toxic and abundant material on Earth [Glunz et al., 2012].

In order to challenge fossil fuels as a replacement energy source, majority of the work on c-Si solar cells are focused on lowering the cost while simultaneously endevouring to reach efficiencies close to theoretical limit provided [Shockley & Quiesser, 1961].

Many different types of c-Si solar cells have emerged, such as back surface field (BSF) [Mandelkorn & Lamneck Jr., 1990], passivated emitter and rear cell (PERC) [Blakers et al., 1989], PERL [Wang et al., 1990], and DASH [Bullock et al., 2016] in pursuit of a cost-efficient PV devices. Currently, BSF solar cells dominate the market; however, PERC solar cells are expected to exceed BSF and become dominant in the market within ten years [ITRPV, 2018]. Commonly, solar cell designs

include highly doped n+ or p+ layers for effectively separating charge carriers (except DASH where carrier selective contacts are used) and transparent conductive electrodes (TCEs) for transporting the carriers from emmiter to the metal contact.

2.3.1. Transparent Conductive Electrode

Transparent electrodes are utilized in optoelectronic devices for the functionalities they provide, such as semi-transparency, flexibility, conductivity etc. Although a variety of transparent electrodes that employs materials like nanowires, metal grids and hybrid structures with dielectrics are developed, transparent conductive oxides (TCOs) are, historically, the most commonly used transparent electrodes in optoelectronic devices [Morales-Masis et al. 2017].

To be utilized in solar cells, TCEs should provide transparency to light in 300-1200 nm wavelength range, while also enabling large area carrier transport without significant resistive losses. In addition to these, a good work function matching with the adjacent layers to get low contact resistance [Klein et al., 2010], uniform deposition methods, enhancement of light coupling into the active layer of the solar cell [Müller et al., 2004] and a large band gap (> 3eV) are expected properties from TCEs in solar cells.

Indium tin oxide (ITO), fluorine-doped tin oxide (FTO) and zinc oxide (ZnO) doped with various materials are examples to materials that are both transparent and conductive [Kim et al., 2016; Minami, 2005], thus, used as TCO electrodes in solar cells. In addition to these, using conductive but not transparent materials, such as metals, as a very thin layer or arranging them as a mesh of nanowires, and using hybrid structures of dielectrics and metal nanowires are other approaches to be used as electrodes [Morales-Masis et al., 2017], as mentioned above.

Among these materials and structures ITO can be considered as the most common material to be used as transparent electrodes in solar cells, due to its excellent optical and electrical properties [Hecht et al., 2011]. However, indium is a rare element on earth and this scarcity makes the utilization of ITO layers increase the fabrication

cost of solar cells. Although the most cost increasing factor of c-Si solar cell fabrication is the fabrication of the Si wafer itself, cost of other processes and used materials are still considered significant and needed to be reduced for PV to replace other energy sources. Hence, alternatives to ITO as TCEs in solar cells are being investigated.

2.3.2. Dielectric/Metal/Dielectric Multilayers

Structures that employ an extremely thin metal film that is sandwiched between two dielectric layers, are one of the alternative transparent electrode types that could replace ITO layers in solar cells [Ellmer, 2012], due to their ability to provide good optical transparency and high conductivity. The thin metal layer in these Dielectric/Metal/Dielectric (DMD) structures renders the charge transport while the dielectric layers, for which metal oxides are commonly utilized, enhances the transparency due to their high refractive index [Sharma et al., 2017].

Table 2.1. *Transmittance at 550 nm of TiOx/Ag/TiOx [Wu et al., 2013], V2O5/Ag/V2O5 [Shen et al., 2011], ZTO/Ag/ZTO and ITO [Winkler et al., 2011] transparent conductive electrodes.*
**MoOx/Ag/MoOx TCE fabricated in this thesis with highest transmittance is also included.*

TCE	Transmittance at 550 nm (%)
$TiO_x/Ag/TiO_x$	87
$V_2O_5/Ag/V_2O_5$	90
ZTO/Ag/ZTO	85
ITO	85
*$MoO_x/Ag/MoO_x$	78

Main advantages of the DMD electrodes that has Oxide/Metal/Oxide (OMO) structure are that they can be fabricated via simple deposition methods at room temperature like thermal evaporation, and cheaper materials than ITO can be used to get similar properties. In addition, the optical and electrical properties of such structures can be tuned by varying the thickness of layers, which is also a significant

feature of these structures. Comparison of transmittance at 550 nm for 60 nm ITO electrode [Winkler et al., 2011], DMD electrodes with similar total thickness [Wu et al., 2013; Shen et al., 2011; Winkler et al., 2011] and HTTCE with highest transmittance and similar total thickness fabricated in this work are given in Table 2.1. Utilization of DMD electrodes [Guo et al., 2015], especially with OMO structures [Han et al., 2008; Wu et al., 2013; Shen et al, 2011], have been studied extensively for these reasons.

2.3.3. Carrier Selective Contacts

Carrier selective contacts, as their name suggests, are utilized in solar cells for the purpose of separating the charge carriers effectively and transporting a type of carrier towards their respective contacts. In other words, carrier selective contacts are requiered to have a selective conductivity that is higher for one type of carrier (either holes or electrons), while being low for the other type, to prevent similar extraction of both minority and majority carriers, which would result in recombination at the electrode. Hence, these contacts should have low minority carrier recombination and efficient majority carrier transport [Feldmann et al., 2014].

Several methods exist for constructing a carrier selective contact [Melskens et al., 2018], of which, the most common one is the utilization of heavily doped Si in homojunction c-Si solar cells. This method relies on the reduction of minority carrier conductivity in the doped region, due to reduced minority carrier mobility and reduced equilibrium concentration of minority carriers caused by difference of doped layers chemical potential with that of the c-Si bulk.

A second method to construct a carrier selective contact works through modification of surface carrier concentrations by implementing either a material with high fixed charge density (Q_f) or a metal oxide with high work function, to the c-Si bulk. By increasing the concentration of one type of carrier in the surface, a band bending of c-Si energy bands can be induced, such that the conductivity of that type of carrier through the contact is also increased.

A third approach is to form a heterojunction with a wide band gap material, that is conductive to the majority carrier type and that has suitable fermi level allignment with bulk c-Si, such that a formation of potential barrier to majority carriers is prevented while simultaneously, a barrier is induced for minority carriers due to large band gap. A common example that utilizes a combination of the second and third approach is silicon heterojunction solar cells that employs doped hydrogenated amorphous silicon (a-Si:H) and c-Si contact, where doped a-Si:H provides carrier selectivity via workfunction-induced band bending while simultaneously creating a barrier to minority carriers with its larger band gap compared to c-Si [De Wolf et al., 2012; Melskens et al., 2018].

Final method of forming a carrier selective contact is to employ an ultrathin tunneling layer that has asymmetrical tunneling probability for each type of carrier, which can occur by reasons like different potential barrier heights and tunneling effective mass. SiO_2 [Ng & Card, 1980] and Al_2O_3 [Nemeth et al., 2016] are example tunnel oxides for carrier selective contacts with the described formation [Melskens et al., 2018].

2.3.4. Dopant-free Solar Cells

Although commertially available solar cells make use of doped layers for carrier selectivity, these layers cause optoelectronic losses in the device, such as parasitic absorption, auger and SRH recombination, and resistive losses [Bullock et al., 2016]. In addition, doping is a high temperature process, which increases the fabrication cost of solar cells. To tackle these problems, doping-free carrier selective contacts with simple deposition methods are being investigated for fabricating completely dopant-free solar cells; for which, several examples are demonstrated in recent years.

Bullock et al., have introduced a dopant-free asymmetric heterocontact (DASH) solar cell architecture that reaches an average efficiency of 19% by using MoO_x as hole selective layer and LiF_x as electron selective layer, together with

hydrogenated amorphous silicon (a-Si:H(i)) passivating interlayers to decrease surface recombination [Bullock et al., 2016]. MoO_x is used as the hole selective layer, whereas three alkali metal fluorides (AMFs) are investigated to be used in electron selective contacts. Although all three AMFs exhibited high workfunction difference with MoO_x, LiF_x stood out with its higher stability of low contact resistivity compared to the rest of considered AMFs. Hole selectivity of MoO_x is further explained in section 2.3.5. The DASH cells were fabricated with simple low-temperature steps without the use of complex alignment or photolithography, which is one of the notable benefits of this cell architecture.

A different dopant-free solar cell with carrier selective contacts is fabricated by Um et al., which has a structure that implements both of the selective contacts on the rear side of the cell and nanoholes on the front side, which are formed by metal-assisted chemical etching to reduce reflection on the front surface, instead of a solar cell design with microscale pyramidal structures with contacts at the front and back [Um et al., 2016]. The high Auger recombination and surface recombination caused by large p-n junction areas of highly doped Si layer, can be reduced significantly by integration of all back contact (ABC) technology into nanostructured Si solar cells; since the device front surface is protected from doping during the ABC fabrication and only the back surface where the contacts are formed, is doped. Also, the shading loss from the front contact is prevented, since both the emitter and BSF contacts are interdigitated at the rear surface. However, the conventional ABC solar cell fabrication is very expensive due to the complexity of the fabrication of interdigitated back contact. The emitter and BSF layers should be formed separately with high-temperature doping processes using diffusion masks fabricated via patterning technology. Um et al. employed an alternative low-cost fabrication strategy that applies dopant-free, carrier selective contacts to the rear side of nanostructured Si solar cells. For carrier selective contacts, MoO_x (hole selective) and LiF (electron selective) were used because of their simple and direct deposition processes at room temperature and the carrier selective properties that they exhibit. In total, six process steps were

bypassed in the fabrication of dopant-free ABC solar cells, including the SiO_2 deposition, photolithography, the SiO_2 etch-back process, and the thermal doping process, which are required for the fabrication of conventional ABC solar cells. This simplification of the fabrication process resulted in significant reduction of the fabrication cost of ABC solar cell, and a power conversion efficiency of 15.4% is reached with this dopant-free ABC solar cell design [Um et al., 2016].

Another example of dopant-free solar cells that implements the contacts on the rear side is given in the work of Wu et al. [Wu et al., 2016b]. In this study, three dopant-free interdigitated back contact (IBC) solar cells implementing various transition metal oxide hole selective emitters were compared in terms of interfacial recombination and the contact resistance. Cs2CO3 was used as electron selective BSF in all of the fabricated cells, and the front side of the cells had a pyramid textured structure with antireflection coating. An efficiency of 16.6% was achieved with vanadium oxide (VOx) emitter.

Above mentioned example studies show the potential of dopant-free solar cells to reach high efficiencies as they gave promising power conversion efficiencies with cost-effective designs.

2.3.5. MoO_x as a Dopant-Free Hole Selective Contact

Transition metal oxides that have high work function, such as vanadium oxide (V_2O_x, $x<5$) [Almora et al., 2017], tungsten oxide (WO_x, $x<3$) [Bivour et al., 2015] and molybdenum oxide (MoO_x, $x<3$) [Battaglia et al., 2014a] have been successfuly utilized as hole selective contacts for solar cells. Among these hole selective layers, MoO_x has the lowest melting point that supports maintaining a high oxidation state and enables easier evaporation of the material, which is an advantage since the contacts are usually formed via thermal evaporation of these metal oxides [Bullock et al., 2014].

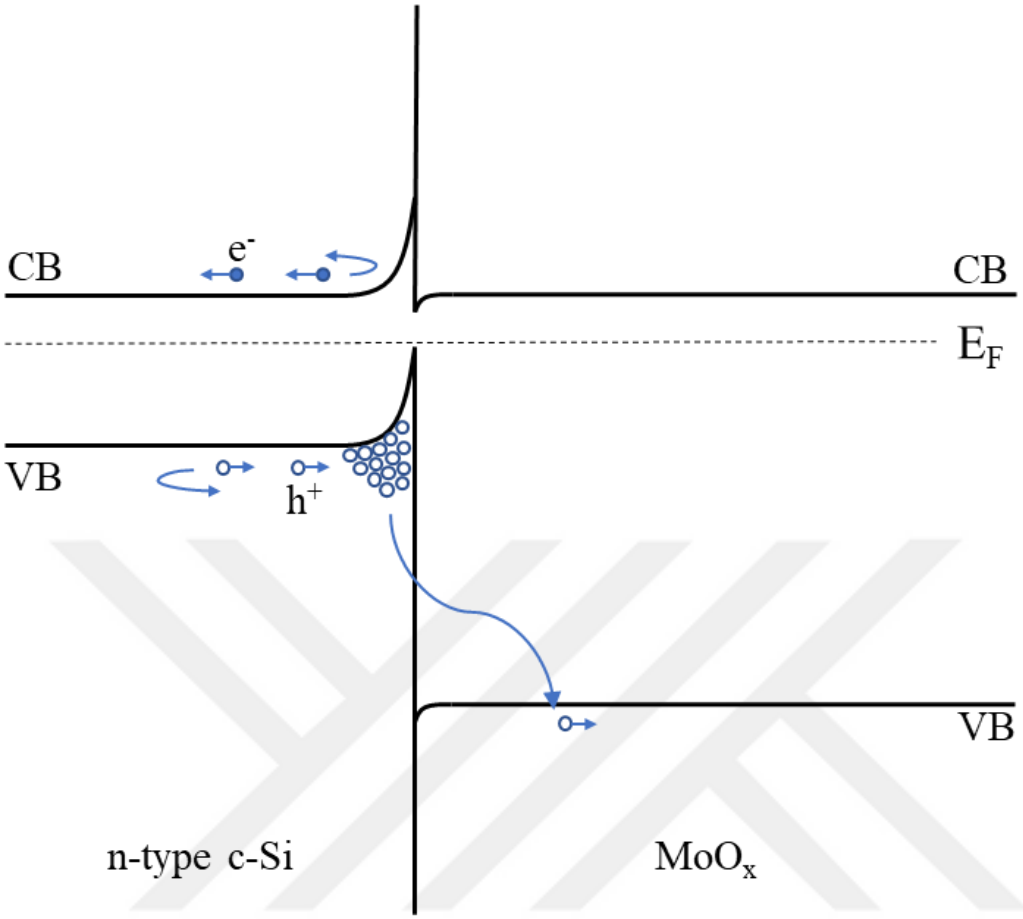

Figure 2.4 Schematic band diagram of n-type c-Si/MoOx contact.

The hole selective behaviour of MoO_x contact has been proven in studies implementing it on n-type c-Si with [Battaglia et al., 2014a] and without [Battaglia et al., 2014b; Bullock et al., 2014] passivating layer between c-Si and MoO_x. In an n-type c-Si/MoO_x contact, the large work function difference between c-Si and MoO_x induces a band bending that depletes the c-Si's surface from majority carriers, which are electrons in this case; thus, formation of contact acts as a quasi-p-type contact [Gerling et al., 2016]. A representation of n-type c-Si/MoO_x contact is given in Figure 2.4.

Mollybdenum trioxide (MoO_3) is a wide band gap material that has a large electron affinity around 6.7 eV. Thermal evaporation of a solid MoO_3 results in sub-stoichiometric MoO_x ($x<3$) amorphous thin films having semi-metallic n-type

properties [Bullock et al., 2014]. Decreasing the oxidation state increases the conductivity of MoO_x, while simultaneously decreases the work function and transparency of the material [Greiner et al., 2012], thus a moderately sub-stoichiometric MoO_x preferred as carrier selective contacts. Therefore, MoO_x is considered to be a material that has a high work function value between 5.5 – 6.9 eV, with a wide band gap exceeding 3eV.

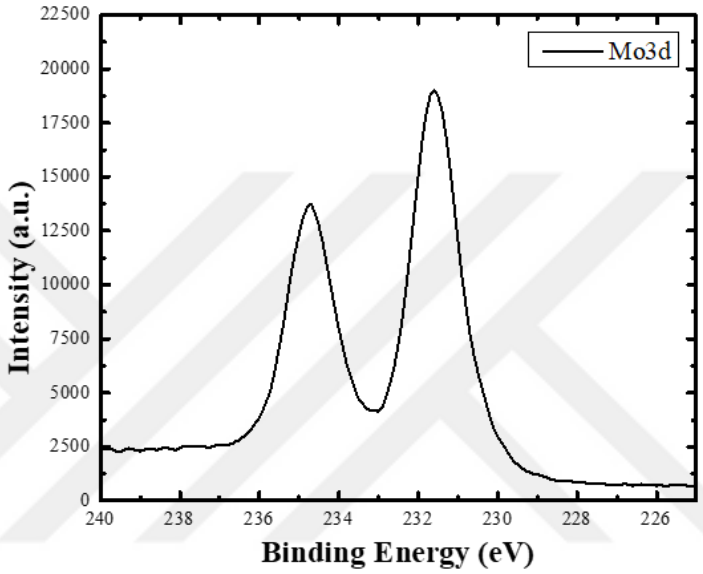

Figure 2.5. Measured Mo3d core level XPS spectrum

Characterizations conducted in our group prior to this thesis on thermally evaporated MoO_x films deposited via the same system and source with identical parameters, showed compositional, optical and structural properties similar to mentioned above. Compositional characterizations via x-ray photoelectron spectroscopy (XPS) revealed that the evaporated MoO_x thin films are sub-stoichiometric and have an atomic concentration ratio ([O]:[Mo]) of 2.7 ± 0.1. The Mo3d core level doublet peak in the measured XPS spectrum given in Figure 2.5. The slightly sub-stoichiometric composition of evaporated MoO_x suggests good hole selective properties, as explained above.

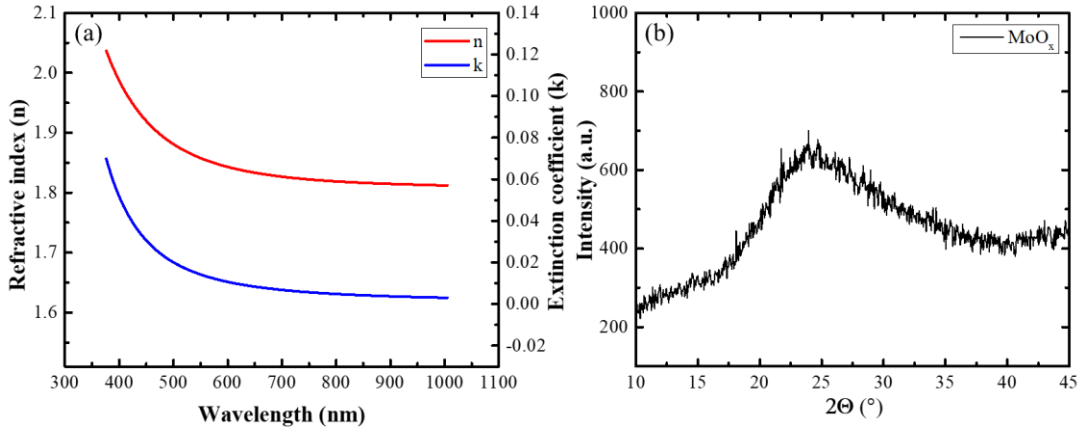

Figure 2.6. (a) Refractive index and extinction coefficient, and (b) XRD spectrum of thermally evaporated MoOx

Optical characterizations by spectroscopic ellipsometry have shown that thermally evaporated 15 nm (± 1 nm) MoO_x have a band gap of 3.3 ± 0.1 eV and a refractive index of 1.8 ± 0.1 at 632.8 nm wavelength light. The refractive index (n) and extinction coefficient (k) of evaporated MoO_x film within 375 – 1100 nm wavelength range is given in Figure 2.6 (a). Also, x-ray diffraction (XRD) spectra for evaporated MoO_x is given in Figure 2.6 (b). Single crystal MoO_3 is shown to have sharp XRD peaks around 13°, 26° and 39° [Battaglia, 2014b]. Although there is a broad peak around 25°, the characterized MoO_x thin film does not exhibit any sharp peaks, which suggests that the thin film has amorphous structure, as expected from thermally evaporated MoO_x.

Due to above mentioned properties of thermally evaporated MoO_x, which are proven in both literature and with the characterizations done before this thesis, it is chosen as the material to be utilized in HTTCE multilayers throughout the experiments performed in this thesis work.

CHAPTER 3

EXPERIMENTAL METHODS

The experimental techniques can be grouped in two: fabrication and characterization related techniques. In Sec. 3.1-3.3, HTTCE solar cell fabrication techniques including sample preparation, thin film deposition via thermal evaporation and edge isolation techniques are detailed. In Sec. 3.4-3.6, techniques including electrical, optical and structural characterization are provided. Sec. 3.7 lists the sample sets that are fabricated and studied in this work.

3.1. Sample Preparation

3.1.1. Crystalline Silicon Substrates

In this work, various single crystalline n-type silicon wafers were utilized as substrates for solar cell fabrication. Production of these c-Si solar cells that implement HTTCE multilayers were done by a number of steps as followed:

- **RCA II cleaning:**

First step was to clean the n-type c-Si wafers by RCA II method to remove the metal ions on the wafer. The wafers were rinsed with deionized water (DI) after this procedure, to remove the chemicals left on the surface. RCA II process forms a thin oxide layer on both sides of the c-Si wafer, which is needed to be removed before doping process.

- **HF dipping:**

After RCA II and DI water treatments, wafers were dipped into a diluted HF solution with a concentration ratio of 1:10 (HF:DI), to remove the oxide layer formed by RCA II procedure. Wafers were then dried in N_2 ambient to be ready for doping step.

- **n+ Doping with $POCl_3$:**

To form an n+ layer on n-type c-Si, wafers were doped via phosphorus oxychloride ($POCl_3$) process at 840 °C, with O_2 as carrier gas. This process forms n+ layer on both sides of the wafer, however, n+ layer on single side of the wafer was needed for this work. Therefore, one side of the wafers were treated with KOH to etch n+ layer on that side. After doping process, the wafers had a structure as represented in Figure 3.1.

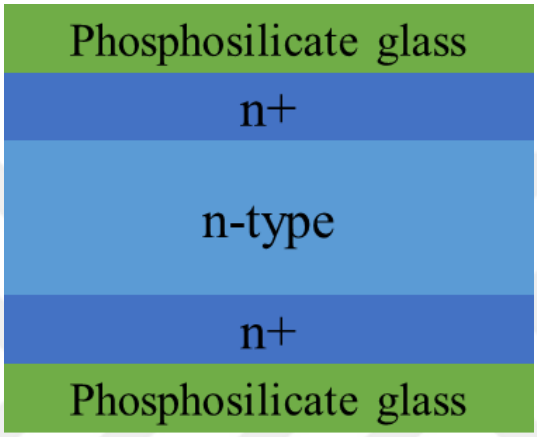

Figure 3.1. Schematic representation of c-Si wafer after doping procedure

- **Single side HF/HCl treatment:**

A special holder, as shown in Figure 3.2, was used to process only one side of the wafers while isolating the other side. Using this holder, wafers were dipped in HF/HCl solution with a concentration ratio of 1:1:10 (HF:HCl:DI) to remove the phosphosilicate glass layer formed after doping process.

Only the oxide layer on one side was removed as a precaution and the remaining oxide layer was left as further protection from a possible leakage of KOH to the isolated side during the next step of wafer preparation, due to the imperfection of the holder.

After dipping in HF/HCl solution, wafers were rinsed with DI to remove remaining chemicals and dried in N_2 ambient before KOH etching on single side.

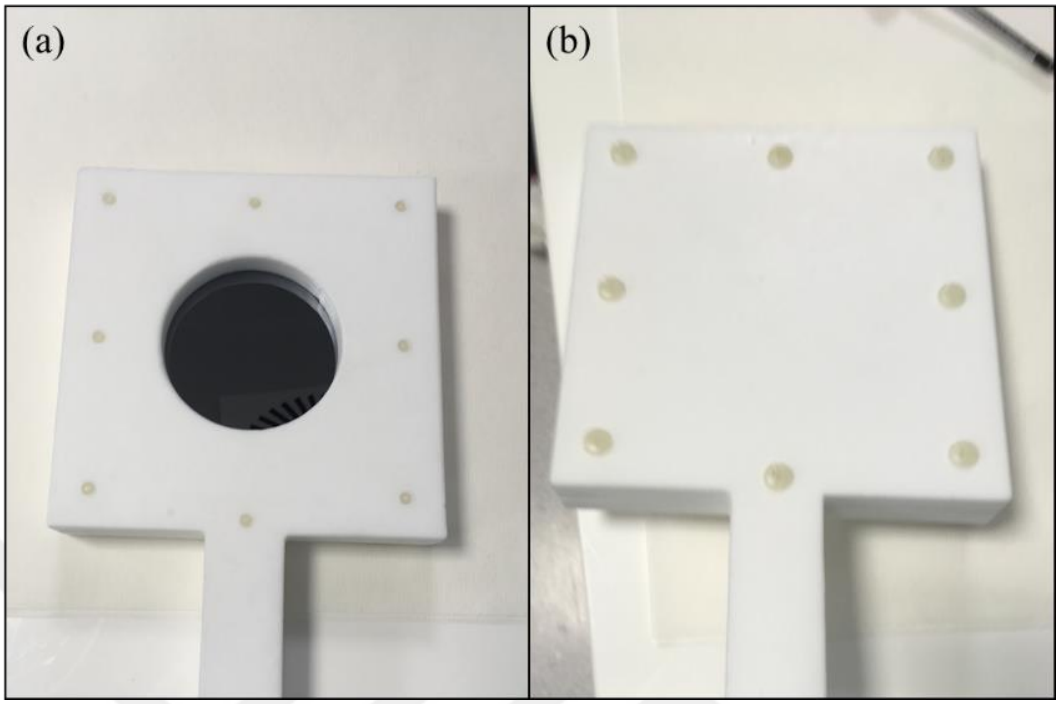

Figure 3.2 Front side (a) and rear side (b) of the special holder for isolating one side of wafer

- **Single side KOH etching:**

The side that was previously treated with HF/HCl solution was etched via KOH solution with concentration ratio of 1:1 (KOH/DI) at 80 °C for 7 minutes, using the same special holder shown in Figure 3.2. KOH etching removed the highly doped n+ layer from one side of the c-Si wafers.

After removal from KOH solution, the wafers were immediately dipped in DI, followed by dipping in HCl solution with concentration ratio of 1:10 (HCl:DI), to stop the reaction of KOH with the surface.

- **HF/HCl and RCA II:**

The wafers were taken out of the holders and dipped in DI, followed by dipping in HF/HCl solution (1:1:10) and DI again, to be prepared for RCA II procedure. RCA II procedure was done one more time, to remove any metallic ions formed on the surfaces after previous treatments. At this point, wafers had a structure similar to the schematic in Figure 3.3.

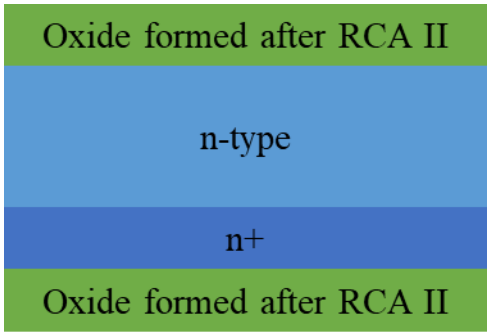

Figure 3.3 Schematic representation of c-Si wafers after second RCA II treatment

Before depositing a rear contact, wafers were dipped in diluted HF solution (1:10) to remove the oxide layers formed after RCA II, followed by dipping in DI and drying in N_2 ambient.

- **Forming Ag rear contact:**

~25 µm thick full area Ag layers were screen printed on n+ side of wafers to form a back contact.

- **Single side HF treatment:**

Before depositing HTTCE multilayer, front side of the wafers were treated with diluted HF solution (1:10) by using a pipette with careful handling, paying special attention not to let any HF to reach the rear side of the wafers. After HF treatment, front side was cleaned with DI and dried with N_2 gas.

- **Thermal evaporation of HTTCE and metal finger:**

HTTCE multilayer and Ag metal fingers were deposited on the front side via thermal evaporation and solar cells with the structure in Figure 3.4 were fabricated. This method is explained in detail in section 3.2. The fabricated solar cells were electrically and optically characterized.

Some characterizations on samples with c-Si substrates did not require a full cell structure. For those samples, certain steps like back contact formation by metallization and front metal finger depositions were not performed. A design that employs Ag fingers within the HTTCE structure is also tested in this work.

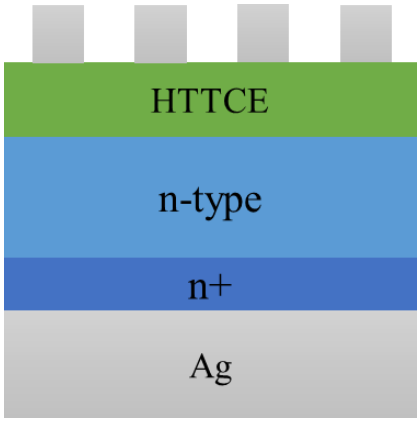

Figure 3.4 Schematic representation of c-Si solar cells employing HTTCE

3.1.2. Corning Glass Substrates

Corning glass substrates were prepared by three solvent cleaning before thermal evaporation of HTTCE multilayers on their surface. First, the glass substrates were cleaned with DI and dried with N_2 gas. Second step was acetone treatment in ultrasonic bath for 10 minutes, to remove organic contaminants from the surface. After that, glass substrates were cleaned with isopropanol alcohol to remove contaminants related to acetone and to remove further organic residues left on the surface. Finally, substrates were dried in N_2 ambient.

After three solvent cleaning, HTTCE multilayers were deposited on the surface by thermal evaporation on these glass samples for transmission measurements. Thermal evaporation process and transmission measurement are explained in detail in sections 3.2 and 3.5.1, respectively.

3.2. Thermal Evaporation

Thermal evaporation is a physical vapor deposition method, which is based on evaporation of source material in vacuum environment, less than 10^{-5} torr pressure, by applying an external voltage to the resistive boat that is holding it. Current passing through the resistive boat heats it and evaporates the source material on it. The vapor particles of the source travels under low pressure to the target substrate surface, where they condense and form a thin film on the surface. Figure 3.5 shows the schematic representation of a thermal evaporation system.

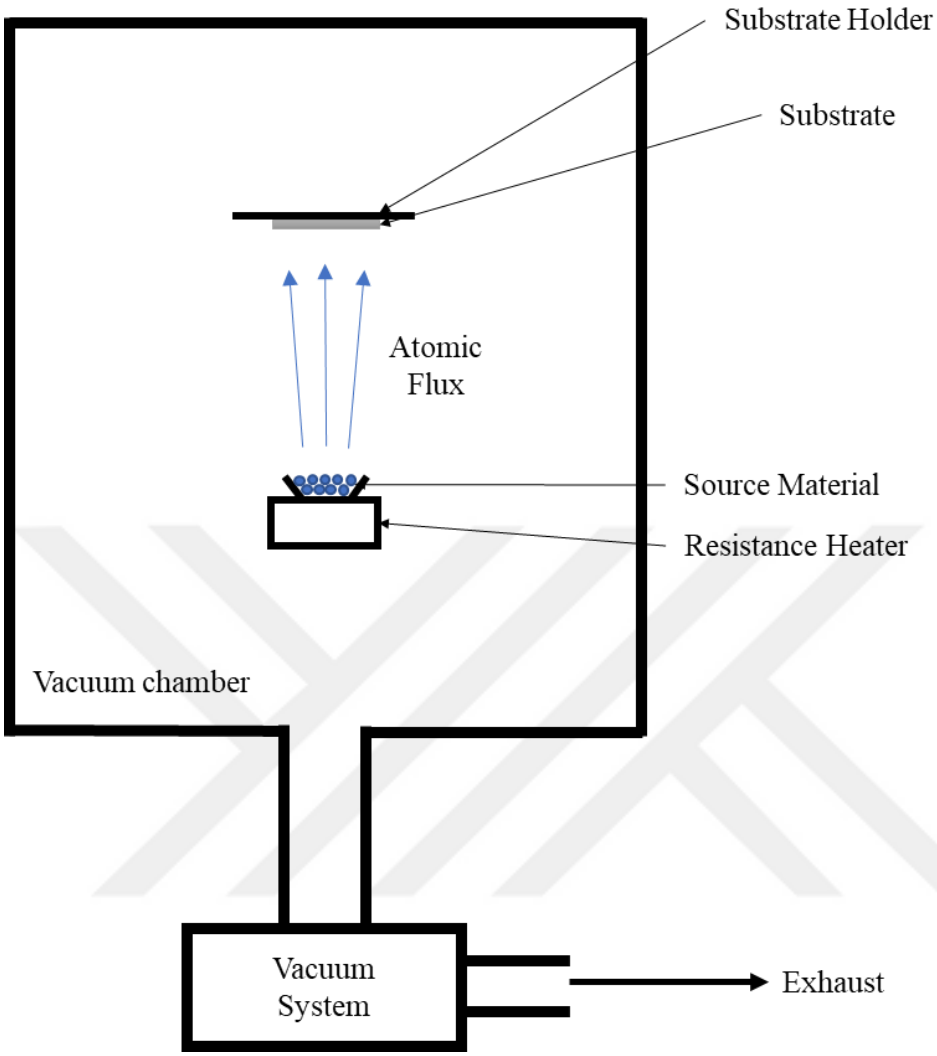

Figure 3.5 Schematic representation of a thermal evaporation system.

3.2.1. System Design

In this work, NANOVAK NVTH – 460T thermal evaporation system was used to deposit MoO_x/Ag/MoO_x HTTCE multilayers on c-Si and glass substrates. The system shown in Figure 3.6 consists of a mechanical and a turbo pump to provide vacuum environment, a power supply to apply voltage on the resistive boats, a chiller for water cooling the copper feedthroughs that holds the resistive boats, a vacuum chamber and a tablet computer with a software inside to monitor and control the deposition process. Inside the vacuum chamber, there are two resistive boats to put

the source materials, a substrate holder which is connected to a rotation motor, a quartz crystal sensor to monitor the deposition rate and thickness of deposited layers, a shutter between substrate holder and resistive boats to start/stop the deposition on surface at the desired rate and time.

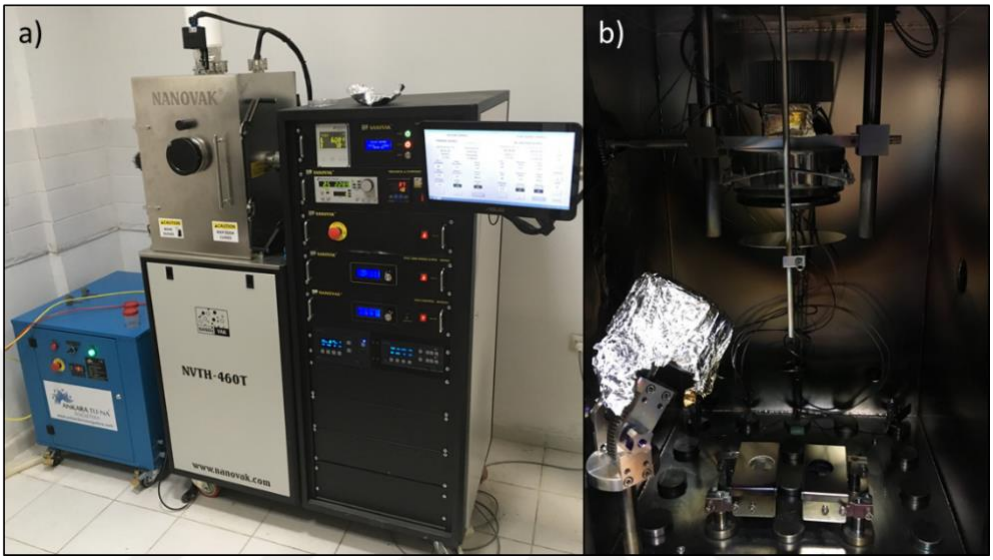

Figure 3.6 Thermal evaporation system. (a) The whole system and (b) the vacuum chamber.

3.2.2. Deposition of MoOx and Ag thin films

At the start of every deposition process, 99.99% pure MoO_3 powder were placed on molybdenum boat and 99.99% pure Ag pieces were placed on tungsten boat. Samples were prepared as described in previous sections and placed on substrate holder inside the vacuum chamber. The chamber was then put under high vacuum via mechanical and turbo vacuum pumps. When a pressure of ~10^{-6} torr was reached inside the chamber, a voltage was applied on the resistive boat of the desired material. MoO_x thin films were deposited at a rate of 0.7 Å/s and different deposition rates of Ag layers ranging between 0.5-2 Å/s were considered. Ag metal fingers as front contact for solar cells were also deposited via thermal evaporation by putting a shadow mask on the surface of the cell. During the evaporation process, substrate holder was constantly rotating, to ensure uniform thin film deposition.

3.3. Edge Isolation

Thermally evaporated thin films can also be present on the edges of the substrates and for solar cell samples, they can contact the backside of the cell. Therefore, edge isolation is a necessary process to prevent short circuit on solar cells after thermal evaporation. In this work, edge isolation is performed via laser marking with a nanosecond laser. Marking the edges of the cell samples with laser beam, by going over them several times, made them easier to break in a straight line. Example of solar cell sample before and after edge isolation via laser marking are shown in Figure 3.7(a) and Figure 3.7(b), respectively.

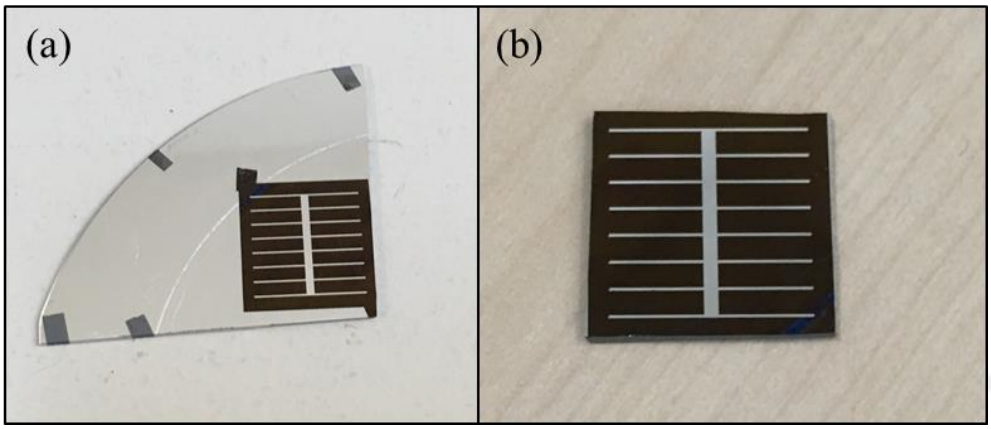

Figure 3.7 Solar cell before (a) and after(b) edge isolation

3.4. Electrical Characterization

3.4.1. I-V Characterization

I-V characterizations are performed by Newport 91192 Solar Simulator in this work, to measure V_{oc}, I_{sc} and FF of the solar cells. For measuring these parameters, the sample is put on a copper plate and two probes are used to connect the sample to current-voltage source. One of the probes is in contact with the metal fingers on the front side of solar cell and the other one is in contact with the copper plate which the rear side of the sample is contacting. The light source of solar simulator, that simulates the sun light, shines light on the sample. The solar simulator and current-voltage

source are connected to a computer, which has a software that measures the I-V characteristics of the solar cell.

P_{in} in Eq. 2.8 depends on the area of the solar cell, since it is calculated as the product of light intensity (light with 1000W/m^2 intensity is used for this work) and area of the solar cell. Since, area of the cell is not a reliable parameter for this study, Eq. 3.1 is used for calculating η, where the unit of V_{oc} is Volts and J_{sc} is in A/m^2.

$$\eta = \frac{V_{oc} * J_{sc} * FF}{1000\ W/m^2} \tag{3.1}$$

3.4.2. Quantum Efficiency Measurement

In this work, quantum efficiency measurements were conducted via Bentham PVE300 Photovoltaic Characterization system. The system consists of tunable light source based on xenon-quartz tungsten halogen dual source, a monochromator to control the wavelength of light focused on the sample, a lock-in amplifier to minimize the noise, optical lenses to guide and focus the light on the sample, a metal platform that holds the sample while making a contact with the rear side of the solar cell, a probe to contact the metal fingers on the front side of the solar cell and a computer that has a software (BenWin+) for controlling the measurement setup and analyzing the measured data. The platform that holds the sample is located inside a chamber which is kept completely dark except the light that is focused on the sample, during the measurements. Figure 3.8 shows the setup inside the chamber during an EQE measurement. An integrating sphere and a mirror can also be seen in this figure. These parts are related to reflectance and transmittance measurements, which are also done with this system, and they are explained in the related optical characterizations section 3.5.1.

To measure EQE, first the beam power of the focused light is characterized by a Si and a Ge detector with known responsivities. Si detector detects light in 300 - 1100 nm wavelength range and Ge detector detects at 800 – 1800 nm wavelength range. After characterizing with both detectors, a calibration file is formed from both,

via the BenWin+ software. The calibration file is then used by the software for analyzing measured data.

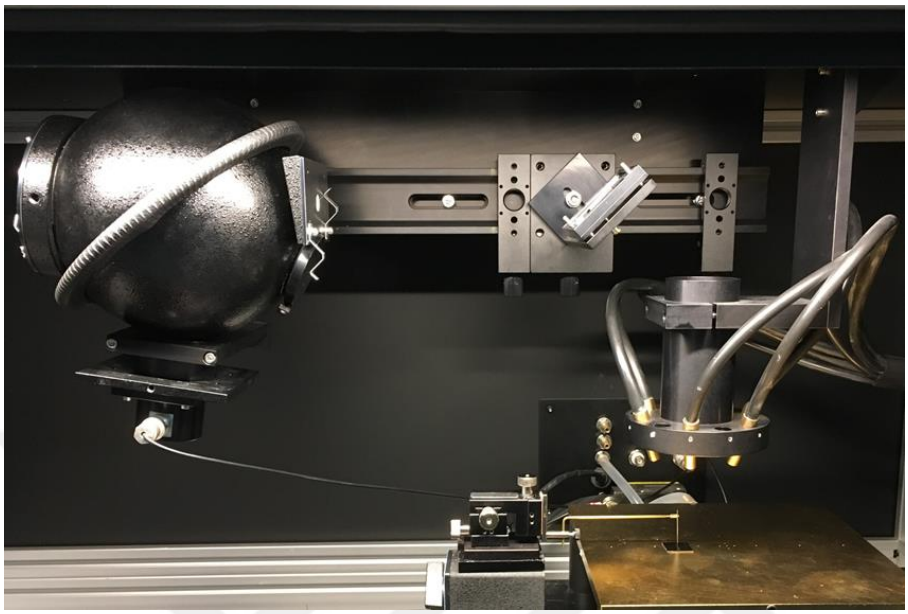

Figure 3.8 EQE measurement setup inside the dark chamber

EQE measurements are done between 300 – 1200 nm wavelength range, by focusing the light on the active area between two metal fingers of the solar cell, which is placed on the metal platform. Probe is contacted to the busbar of the cell and the measurement is done by recording the photogenerated current as a function of wavelength. The software then, calculates EQE from the measured data. To obtain IQE, Eq. 3.2 is used, where R is the reflectance of HTTCE deposited on c-Si surface, measured prior to the calculation.

$$IQE = \frac{EQE}{1-R} \qquad \text{Eqn. (3.2)}$$

However, this IQE calculation does not include the parasitic absorption caused by the HTTCE structure, before the photons reach the junction and absorbed there. Therefore, the IQE results given in this work are affected largely by the parasitic absorption, and they are interpreted accordingly.

3.4.3. Sheet Resistance Measurement

Sheet resistance (R_{sheet}) is defined as the resistance of the uniform thickness of a thin film. It is an important parameter to know for designing the masks for patterning metal fingers on the front side of the solar cells, to collect the carriers effectively. In this work, R_{sheet} of HTTCE layers deposited on glass substrates were measured via four point probe technique, which is represented in Figure 3.9. Four electrical probes which are separated from each other with equal distances were used. Outer probes applied current while inner probes measured the voltage drop caused by R_{sheet} of the thin film.

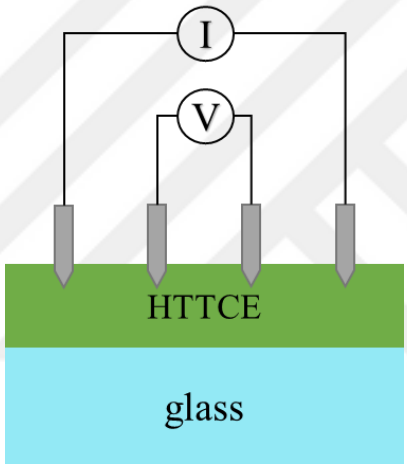

Figure 3.9 Representation of four point probe sheet resistance measurement

3.5. Optical Characterizations

3.5.1. Reflectance, Transmittance & Absorption

Reflectance and transmittance measurements are also done in Bentham PVE300 system. For these measurements, a mirror is used to divert the direction of monochromated light towards the integrating sphere, which has a Si-Ga detector attached that is able to detect a wide range of 300-1800 nm wavelength light, inside the chamber. Before both reflectance and transmittance measurements, a $BaSO_4$ disk is attached to the back side opening of the integrating sphere and reference measurements are taken for a wavelength range of 300-1200 nm. Inside walls of the

integrating sphere are also coated with $BaSO_4$, therefore this reference measurement determines the 100% reflection and transmission conditions. Hence, the optical characterizations of the samples are made respectively to these reference measurements.

Transmittance measurements are done for HTTCE layers deposited on glass substrates. For the transmittance measurement of a sample, the integrating sphere is placed as shown in Figure 3.10(a), to focus the monochromated light beam on the sample, which is attached to the integrating sphere's front side opening. The transmitted light is detected via the detector attached to the integrating sphere, and the software calculates the transmittance of the sample with respect to the reference measurement done when the integrating sphere was at the same position. $BaSO_4$ disc remains attached to the back side opening of the integrating sphere, to keep the transmitted light inside the sphere to be reflected many times and eventually reaching the detector. In addition, optical simulations of transmittance of HTTCEs in one of the sample sets are done via finite element method [Zienkiewicz et al., 2013]

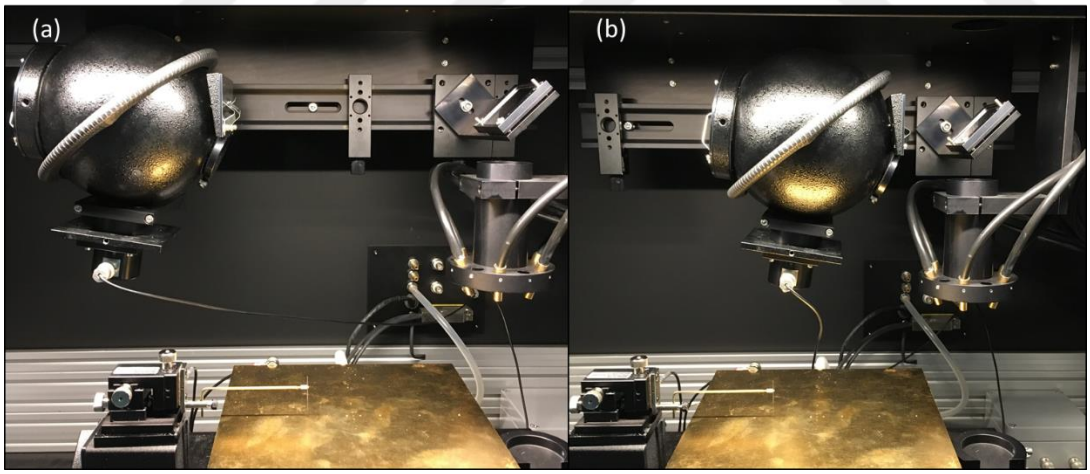

Figure 3.10 Configuration of the setup for (a) transmittance and (b) reflectance measurements

Reflectance measurements are done for HTTCE layers deposited on both glass and c-Si substrates. For the reflectance measurement of a sample, the integrating sphere is placed closer to the mirror, as shown in Figure 3.10(b), to focus the light on

the back side opening. After the reference measurement at that position of the sphere, $BaSO_4$ disc is replaced with the sample and the reflected light from the sample is detected by the detector attached to the integrating sphere. The software, as in the case of transmittance, calculates the reflectance of the sample with respect to the reference measurement.

$$Absorption = 1 - Reflectance - Transmission \tag{3.3}$$

$$X_{weighted} = \frac{\int_{\lambda_1}^{\lambda_2} I_{AM1.5G}(\lambda) X(\lambda) d\lambda}{\int_{\lambda_1}^{\lambda_2} I_{AM1.5G} d\lambda} \tag{3.4}$$

Absorption of HTTCE layers are calculated by the simple formula given in Eq. 3.3. The transmittance and reflectance measurements of HTTCE layers deposited on glass substrates are used for this characterization. In addition, weighted transmission, weighted reflection and weighted absorption of HTTCE structures are calculated, using Eq. 3.4, where $X_{weighted}$ is weighted absorption, transmittance or reflectance, λ_1 and λ_2 are 300 nm and 1200 nm, respectively, representing the measured wavelength range, and $I_{AM1.5G}$ is the 1 sun air mass 1.5 global (AM1.5G) spectral irradiance [Morales-Masis et al., 2017]. AM1.5G spectral irradiance between 300 – 1200 nm wavelength range is given in Figure 3.11.

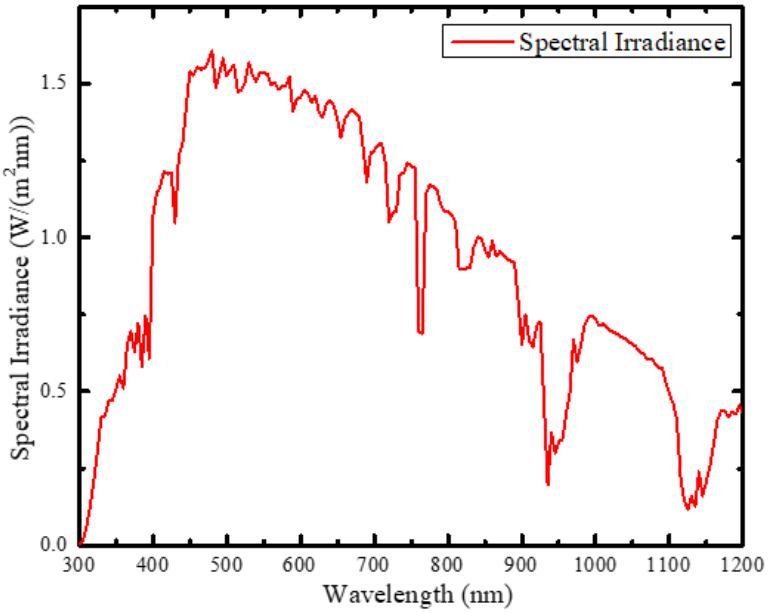

Figure 3.11 AM1.5G Spectral Irradiance between 300 – 1200 nm wavelength range

3.6. Morphological Characterization

3.6.1. Scanning Electron Microscopy

Scanning electron microscopy (SEM) is an imaging technique that scans the desired surface with a focused electron beam and provides informative images by detecting secondary electrons, which are the electrons kicked out from the surface atoms due to collisions with electrons from the focused beam. In this work, SEM images are taken by Zeiss EVO HD15 SEM with a LaB6 filament, to observe the morphology of the surface of samples.

3.7. Sample Sets for Experiments

In this work, 5 sample sets are prepared to compare and characterize for developing the HTTCE multilayers.

- **Sample Set I**

This set consists of sample solar cells with five different n-type c-Si (100) substrates that are listed in Table 3.1. The main difference is the resistivities which implies the doping concentration of the wafers; however, wafers are also different from each other in terms of thickness and surface properties; that is some of them are single side polished (SSP) and some are double side polished (DSP). MoO_x/Ag/MoO_x multilayers are deposited on each wafer with the layer thicknesses fixed to 15nm/10nm/30nm. MoO_x and Ag layers are deposited at 0.7Å/s and 0.5Å/s rates, respectively. Solar Cells made in this set are compared in terms of cell performance, to choose the best c-Si wafer for this study.

- **Sample Set II**

This set is used to optimize Ag deposition rate. Rates of 0.5Å/s, 1.0Å/s, 1.5Å/s and 2.0Å/s were used for Ag and MoO_x deposition rate was fixed on 0.7Å/s. MoO_x/Ag structures were deposited on c-Si substrates and SEM images were taken to observe if the Ag thin films are continuous or not. Solar cells employing MoO_x/Ag/MoO_x HTTCE layers with these different Ag deposition rates were constructed and compared in terms of electrical and optical properties.

Table 3.1. *Properties of n-type c-Si substrates in set I.*

c-Si Wafer	*Measured Resistivity*	*Thickness*	*Surface*
I	0.94 Ω-cm	200±30 µm	DSP
II	1.25 Ω-cm	500±25 µm	SSP
III	3 Ω-cm	275±25 µm	DSP
IV	3.4 Ω-cm	525±50 µm	SSP
V	80 Ω-cm	200±30 µm	DSP

- **Sample Set III**

Samples in this set are solar cells that employs a different HTTCE design. Instead of depositing Ag fingers on top of MoO_x layer, fingers are deposited directly on the Ag layer and then covered by a MoO_x layer, utilizing a shadow mask such that only the bus bar is not covered with MoO_x to be able to get contact on the front side of the cells. So, the structure of HTTCE multilayer is MoO_x/Ag/Ag fingers/MoO_x with layer thicknesses of 15nm/10nm/~250nm/30nm. Performance of the cells are compared to cells with MoO_x/Ag/MoO_x HTTCE.

- **Sample Set IV**

In this set, sample solar cells with HTTCE layers that has different thicknesses of outer MoO_x layer, were compared in terms of electrical and optical properties. A range of thicknesses, from 30 nm to 60 nm of MoO_x were compared for optimization.

- **Sample Set V**

In the final set, textured c-Si substrates were used to make solar cells with HTTCE and comparison of electrical and optical properties, with cells in previous sets which are made from polished c-Si substrates, were done. Textured c-Si substrates were prepared the same way as described in section 3.1.1, only difference was the solution concentration and etching time of KOH etching step during single side etching, to get pyramid textured surface on the front side while also etching the n+ doped region.

CHAPTER 4

RESULTS & DISCUSSION

4.1. Comparison of Different Wafers

This part of the thesis is targeting to provide a survey for observing the effect of use of different wafers in solar cells employing HTTCE. Solar cells employing MoO_x/Ag/MoO_x HTTCE structures with 15nm/10nm/30nm layer thicknesses are fabricated with five different c-Si wafers, which are listed in Table 3.1, and compared in terms of cell performance, mainly by their V_{oc} values, since it is reported that V_{oc} has a relation with the doping concentration of c-Si substrates [Nasser et al., 2017]. First MoO_x layer is used for its hole selective properties and since 15 nm MoO_x in contact with n-type c-Si has been observed to give a V_{oc} of 580 mV [Battaglia et al., 2014b], 15 nm is chosen for the first layer thickness. Ag layer after that is used to get a conductive structure and 10 nm of this layer is chosen due to the proven optical and electrical properties of the Ag thin films at that thickness in studies with similar structure to the HTTCE in this work [Wu et al., 2016a; Nguyen et al., 2012]. Outer MoO_x is used for enhancing the transparency and more importantly, preventing the oxidation of Ag thin film that comes before it. The thickness of outer MoO_x is fixed at 30 nm for this section and the variation on this thickness is studied in section 4.4.

4.1.1. I-V Characterization

Several solar cells were made by each wafer, and comparison of the average V_{oc}, J_{sc}, FF and efficiency values of wafers are shown in Figure 4.1. The x-axis of plots given in Figure 4.1 represents the five wafers listed in Table 3.1. The number of samples characterized for each wafer is denoted as n in Figure 4.1(a). The graphs should be interpreted with a precaution that they are not designed to point certain trends, since the doping concentration is not the only difference these wafers have.

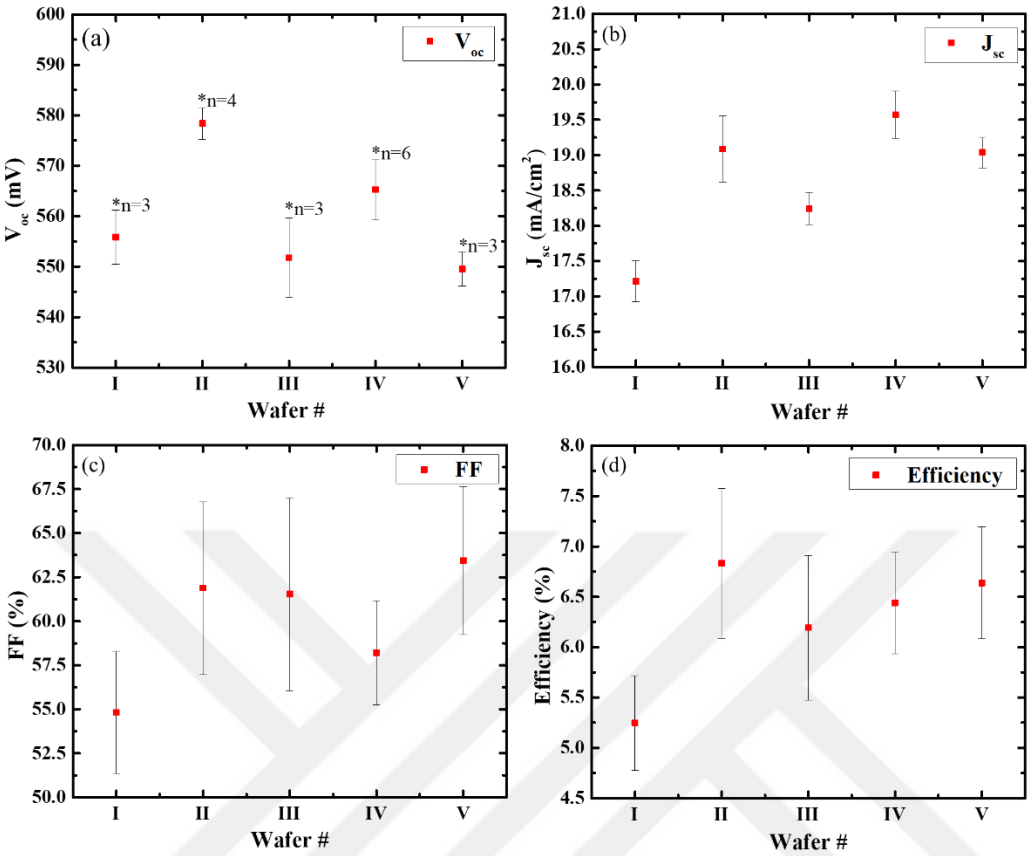

Figure 4.1 Voc (a), Jsc (b), FF (c) and efficiency (d) comparison of different wafers employing same HTTCE structure.

It can be seen from Figure 4.1, that highest V_{oc} values are observed in cells made by wafer II, while for J_{sc} and FF characterizations, wafer IV and V gave better results. Since the differences in J_{sc} and FF are not so severe as they are in V_{oc}, cells fabricated from wafer II resulted with the highest efficiencies.

If all the properties of c-Si wafers were the same except for the doping concentration, it would have been expected to get a trend as increasing performance with decreasing doping concentration up to some point, following by a decrease in performance for lower doping concentrations. Differences in the thickness of the wafers showed importance while forming a back contact, since thinner substrates could not handle the screen-printed Ag contact and obtained a bended form while thick wafers preserved their flat form. Bending made the wafers more brittle and probably

influenced the performance of solar cells fabricated with those wafers. In addition, material defects also have effect on the performance of cells, and the performance differences between cells could also be explained by variations of such defect formations within different wafers.

4.1.2. Quantum Efficiency

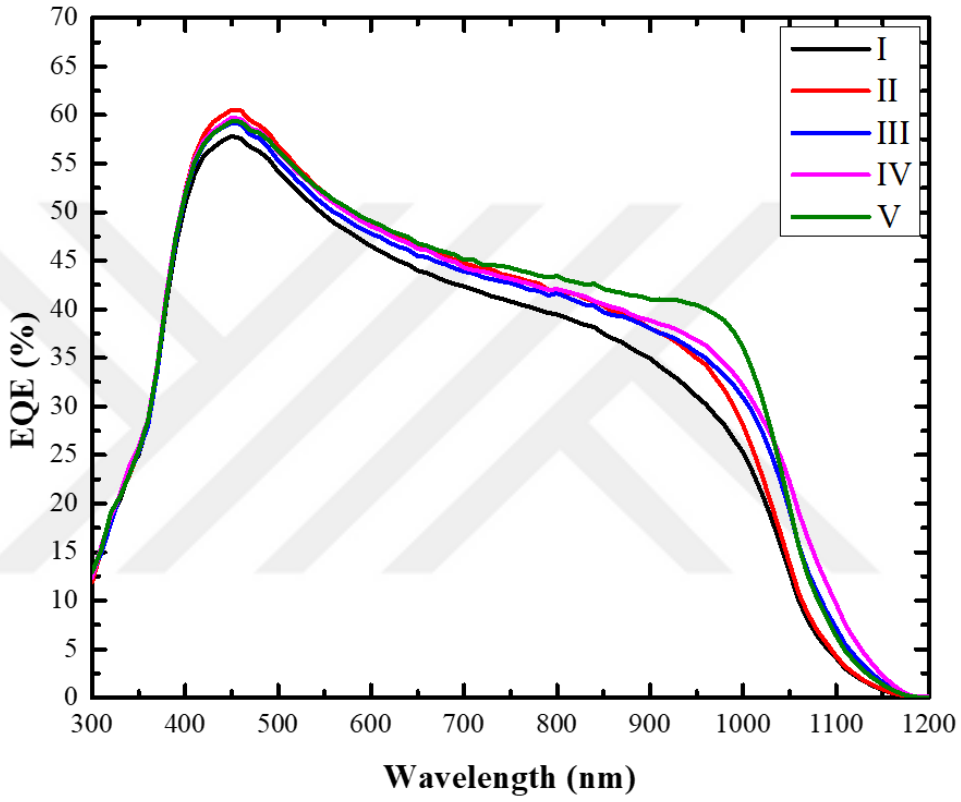

Figure 4.2 EQE of solar cells made with different wafers

Figure 4.2 shows the EQE of solar cells made with different c-Si wafers and it is observed that while wafer II has higher EQE in shorter wavelengths, wafer V and IV seems to have better EQE in longer wavelengths. Despite this EQE comparison, since the highest average Voc and efficiency is observed in wafer II, it has been chosen and utilized as the substrate for the fabricated solar cells in the rest of this work

4.2. Optimization of Ag Deposition Rate

Deposition rate of Ag layer between two MoO_x layers is varied between 0.5-2.0 Å/s and its effect on the morphological, optical and electrical properties of cells employing MoO_x/Ag/MoO_x HTTCE structures with fixed thicknesses of 15nm/10nm/30nm is observed.

4.2.1. SEM Imaging

SEM images of 10 nm Ag thin films, deposited on c-Si/MoO_x (15 nm) with deposition rates of 0.5 Å/s, 1.0 Å/s, 1.5 Å/s and 2.0 Å/s, are taken and shown in Figure 4.3. Special attention is payed in order to following images to represent the general view of the sample. 0.5 Å/s rate resulted in discontinuous island growth of silver and higher rates resulted in more continuous thin film formation. In addition, Ag nanoparticles on the surface are observed for 0.5 Å/s and 1.0 Å/s growth rates.

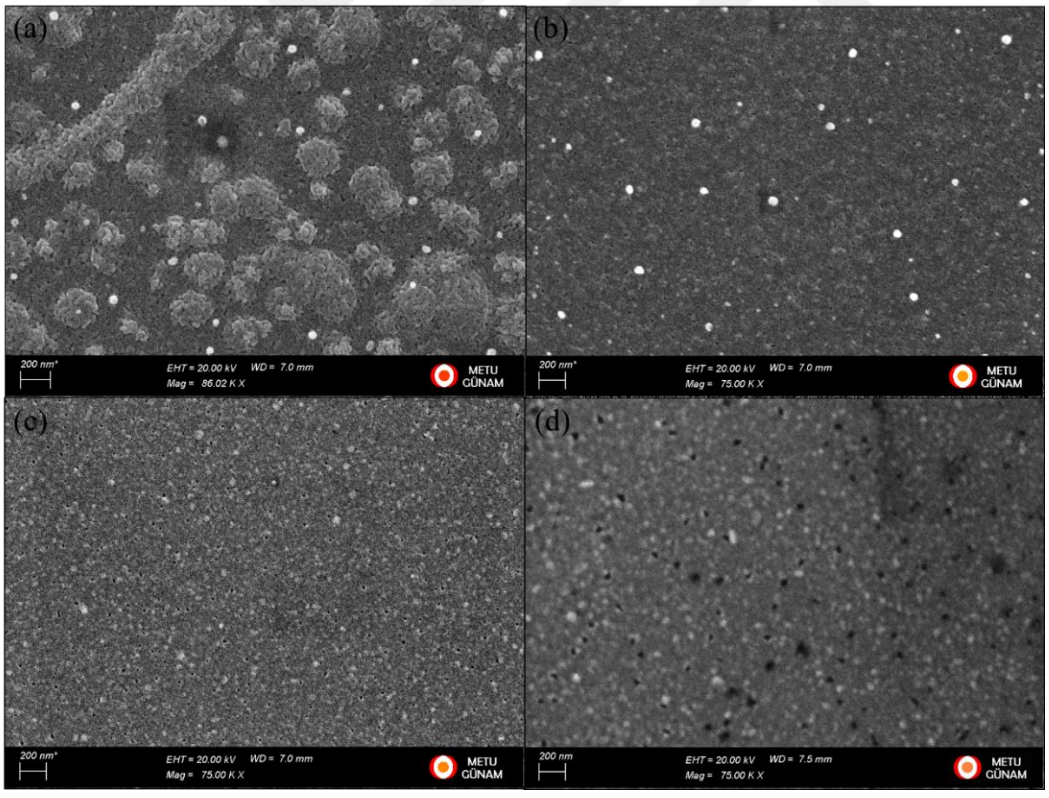

Figure 4.3 SEM images of Ag thin films deposited at (a) 0.5 Å/s, (b) 1 Å/s, (c) 1.5 Å/s and (d) 2 Å/s rates.

The observation of more continuous film formation with higher deposition rates is in correlation with similar studies [Cattin et al., 2013]. An explanation to this behaviour, given by Cattin et al., is that for slow rates, deposited Ag atoms find enough time to diffuse and reorganize which result in discontinuity in the deposited thin film, while for higher rates formation of a high density of nucleation centers in a short time result in continuous film formation.

4.2.1. I-V Characterization

Figure 4.4 shows the I-V characterization results of solar cells fabricated with different Ag deposition rates. Characterization of a reference solar cell that has a 45 nm MoO_x front contact and does not employ a Ag thin layer, is also given in Figure 4.4, where it is labeled as 0 Å/s Ag deposition rate. The number of samples characterized for each rate is denoted as n in the Figure 4.4(a).

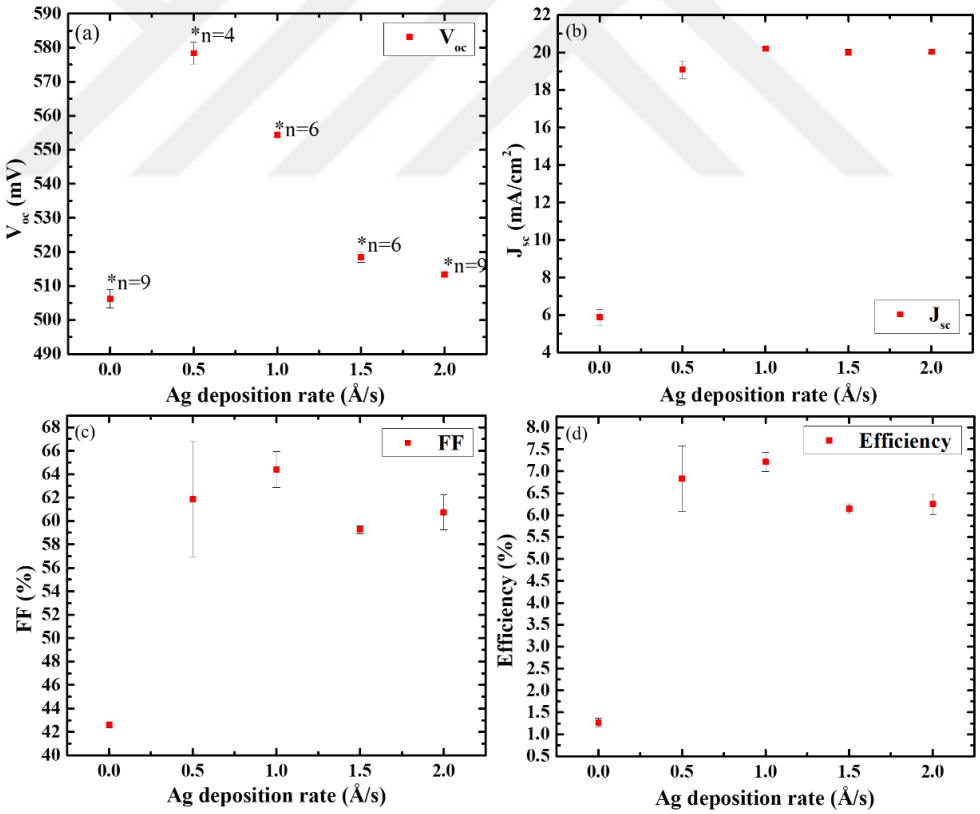

Figure 4.4 (a) Voc, (b) Jsc, (c) FF and (d) Efficiency comparison of solar cells fabricated with different Ag deposition rates

Findings given in Figure 4.4 shows the improvement in carrier collection provided by the Ag thin film, as the reference cell that does not include an Ag thin layer suffers from very low J_{sc} and FF, compared to the cells that utilize MoO_x/Ag/MoO_x HTTCE. V_{oc} of the reference cell is also low, which is due to the carrier selective contact being 45 nm of MoO_x that seems to be promoting recombinational losses at that much thickness.

It is known in literature that Ag thermal evaporation starts with discontinuous surface coverage until a certain thickness, after which a continuous film is formed. The thickness at which the continuity is achieved is highly influenced by the deposition rate, as observed in the previous section. In this study the device fabricated with 0.5 A/s Ag deposition rate successfully operates, albeit with low efficiency which is atribured to increased resistance due to discontinuous film formation.

It can be seen from Figure 4.4(a) that increasing the deposition rate had a negative effect on V_{oc}. This negative effect suggests that the Ag atoms damage the first MoO_x layer that is in contact with n-type c-Si, when they are deposited on the surface with higher rates. Moreover, increasing the rate to 1.0 Å/s resulted with a higher J_{sc}; although, further increase of rate did not lead to more enhancement in J_{sc}. From the SEM images where better continuity of Ag thin films are observed in higher rates, and also from the transmittance results given in the next section, enhancement of J_{sc} with increased rate was expected. This distruption of increase can be explained by, again, the damage induced on the junction layer by high rate deposition of Ag, since J_{sc} is related with the photocurrent collected from the device.

In order to hinder the effect of high deposition rate on V_{oc}, while benefiting from the higher transparencies; a mixed deposition rate is utilized for fabricating solar cells with HTTCE. A rate of 1.0 Å/s for the first 5 nm Ag and 1.5 Å/s for the rest until the formation of 10 nm Ag thin film is considered. However, this mixed rate did not give better results in I-V measurements, as the V_{oc} values of the solar cells employing this rate are around 510 mV.

4.2.2. Quantum Efficiency

In Figure 4.5(a), which shows the EQE of different Ag deposition rates, reduction of EQE in short and high wavelengths suggests that there are some recombinational losses present in the front and rear contacts of the solar cells. General reduction in EQE includes reflection losses, therefore IQE of the cells, together with the reflectance of HTTCE structures deposited on c-Si, are given in Figure 4.5(b), to have a better understanding of the cells. From Figure 4.5(b), it seems that IQE increases as the rate increases from 0.5 Å/s to 1.0 Å/s, which is probably caused by the decrease of parasitic absorption in the HTTCE multilayer. It can also be seen from the same figure, that IQE decreases as the rate increases further from 1.0 Å/s to 2.0 Å/s, which implies that either higher rates result in high parasitic absorption, or they cause transport issues for holes in the HTTCE. Solar cells employing the mixed Ag deposition rate which is shown as the green line in Figure 4.5, seems to have an IQE close to solar cells that employ 1.0 Å/s Ag deposition rate. Since parasitic absorption is the dominant effect that reduces the IQE as explained in section 3.4.2, it seems that the HTTCE structures fabricated with the mixed rate and 1.0 Å/s rate has less absorption than the other considered rates in this study.

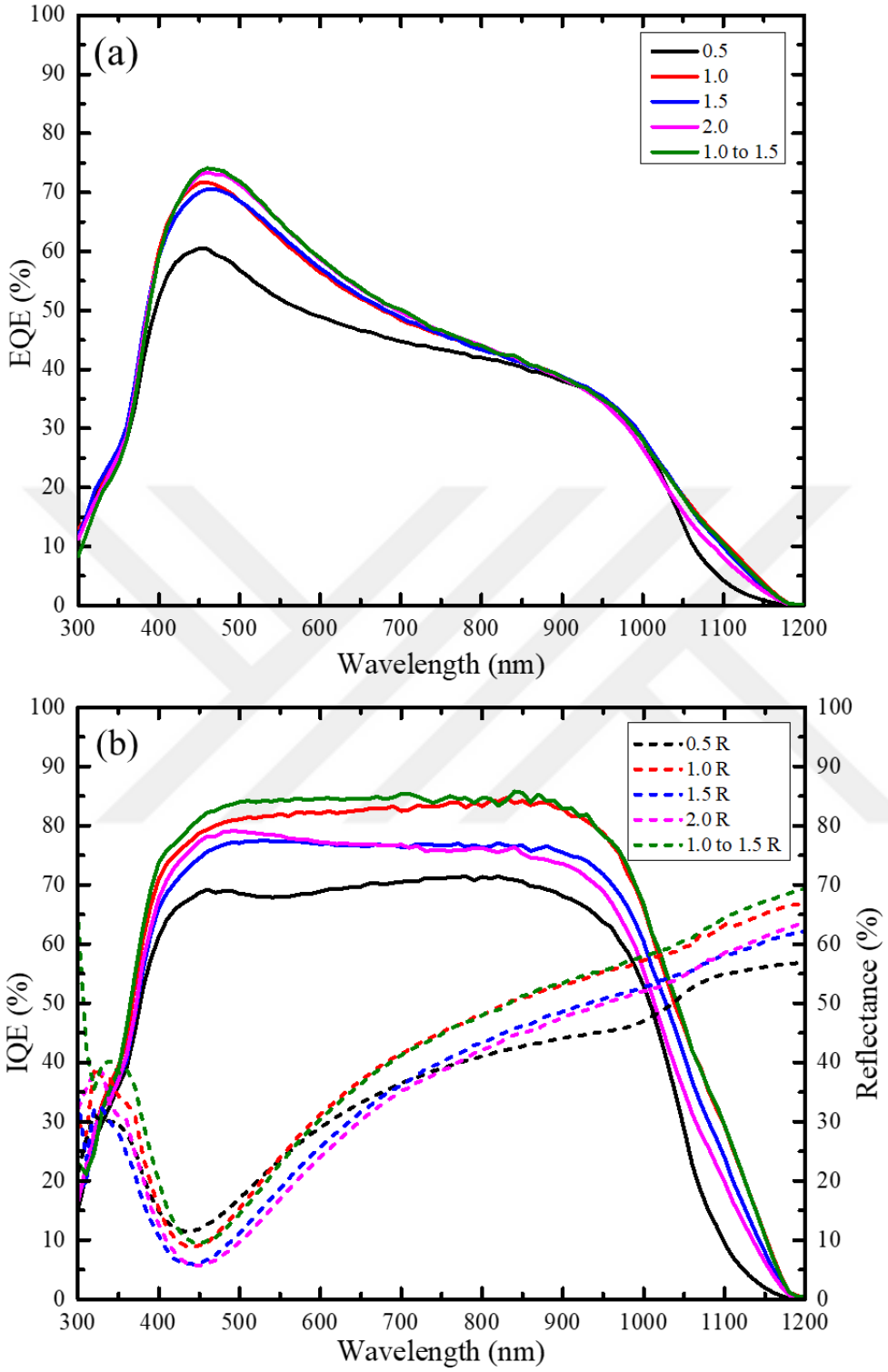

Figure 4.5 (a) EQE and (b) IQE characterizations of solar cells employing HTTCE structures fabricated with different Ag deposition rates. (b) also includes reflectance of HTTCE structures deposited on c-Si.

4.2.3. Sheet Resistance

Table 4.1. *Sheet resistances of HTTCE structures fabricated with different Ag deposition rates*

Ag rate (Å/s)	R_{sheet} *(Ω/sqr)*
0	-
0.5	10.05 ± 0.07
1.0	7.32 ± 0.05
1.5	6.70 ± 0.04
2.0	7.22 ± 0.03
1.0 to 1.5	6.2 ± 0.03

Table 4.1 shows the R_{sheet} of HTTCE structures fabricated with different Ag deposition rates. HTTCE with 0.5 Å/s Ag deposition rate has a R_{sheet} of ~10 Ω/sqr while higher rates have R_{sheet} between 6-7 Ω/sqr. This is in correlation with the finding of continuous film formation in higher rates, from SEM characterizations. It is expected to get higher R_{sheet} in discontinuous island formation than continuous thin films; since, the average path lengths of holes in discontinuous films are larger than continuous films. Moreover, average cross-sectional area of carrier transport channels being small in discontinuous films is another reason for high R_{sheet}. The reference cell had 45 nm of MoO_x and since it is almost an insulator, its R_{sheet} could not be measured with the four point probe technique.

4.2.4. Optical Characterization

Optical characterizations revealed that increasing the deposition rate of Ag layer provides enhancement in transmission (Figure 4.6(a)) of the HTTCE structure, mainly in the visible region while it remains low in longer wavelengths; which is in correlation with the increase of reflection (Figure 4.6(b)) in longer wavelengths. Moreover, a general decrease in absorption (Figure 4.6(c)) is observed with the increase of deposition rate; however, this is not exactly the same finding from the IQE analysis in section 4.2.2, where it is interpreted that HTTCE constructed with 1.0 Å/s deposition rate has less absorption.

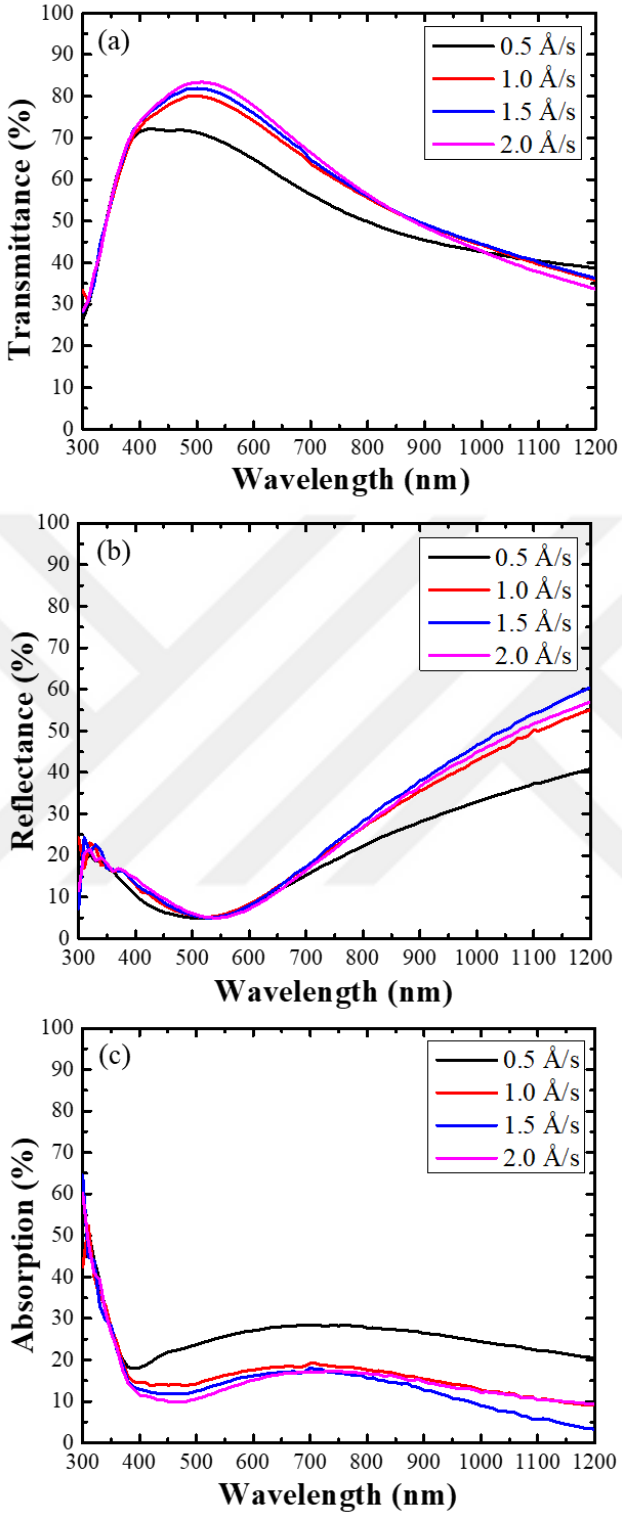

Figure 4.6 (a) Transmittance, (b) Reflectance and (c) Absorption of HTTCE structures with different Ag deposition rates

The optical measurements in the present section are taken from HTTCE deposited on glass; therefore, they are the relative observations of HTTCE structures, and most probably are different for HTTCEs deposited on c-Si substrates. Hence, a complete correlation with IQE measurements, which are largely influenced by parasitic absorption as explained in section 3.4.2, are not expected .

Figure 4.6 (a) and (b) shows that both transmittance and reflectance is higher in HTTCEs made with rates higher than 0.5 Å/s. Moreover, it can be seen from Figure 4.6(c) that parasitic absorption is higher for HTTCE structure with 0.5 Å/s Ag deposition rate, compared to HTTCE structures deposited with higher rates. Higher parasitic absorption might be caused by localized plasmon involvements in the discontinuous film.

The optical properties of HTTCE constructed with the mixed Ag deposition rate are promising, as is shown in Figure 4.6 by the green line, the solar cells employing that rate still suffered from low V_{oc} values of ~510 mV. Therefore, Ag deposition rate of 1.0 Å/s is chosen as the optimum rate in this work; although, further detailed investigations on the rate could pottentially reveal a better parameter.

4.3. A Different HTTCE Design

A second HTTCE design that contains the Ag metal fingers within the MoO_x/Ag/MoO_x structure, by depositing Ag fingers directly on the Ag layer and covering them with a MoO_x layer, is constructed. HTTCEs from the second design, therefore, had a structure as MoO_x/Ag/Ag fingers/MoO_x (M/A/AF/M) with layer thicknesses of 15nm/10nm/~250nm/30nm. Quantum efficiency and I-V measurements are done to compare this design to the original MoO_x/Ag/MoO_x (M/A/M) structure.

4.3.1. Quantum Efficiency

M/A/M and M/A/AF/M HTTCE structures did not show any significant difference quantum efficiency measurements, as can be seen from Figure 4.7. The reflectance data used for IQE is the same for both M/A/M and M/A/AF/M structures,

since light that contributes the photocurrent passes from the same layers for both of them and light that is incident where the Ag fingers are considered as lost.

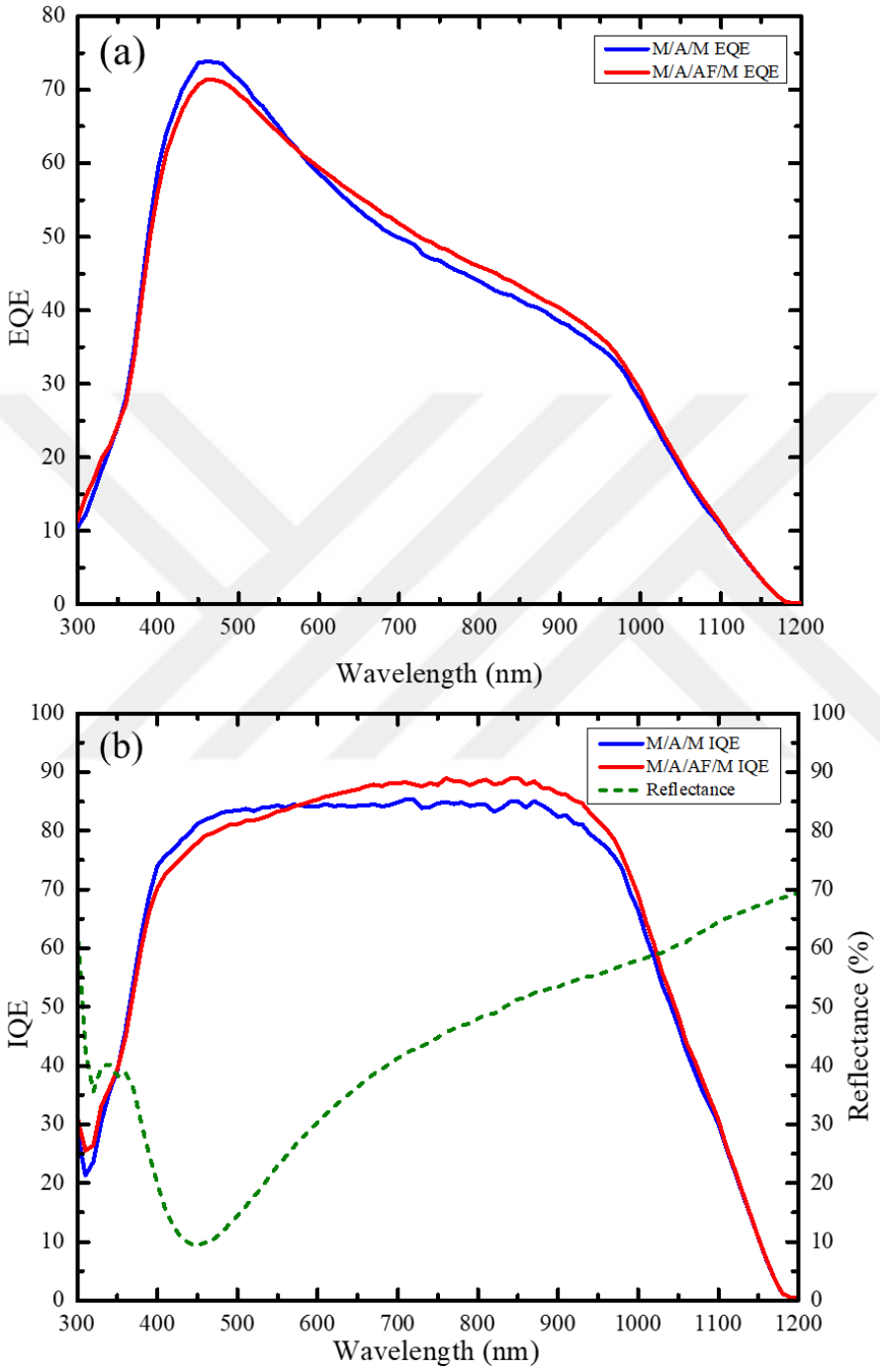

Figure 4.7 (a) EQE and (b) IQE characterizations of solar cells employing HTTCE structures with M/A/M and M/A/AF/M designs.

4.3.2. Electrical Characterization

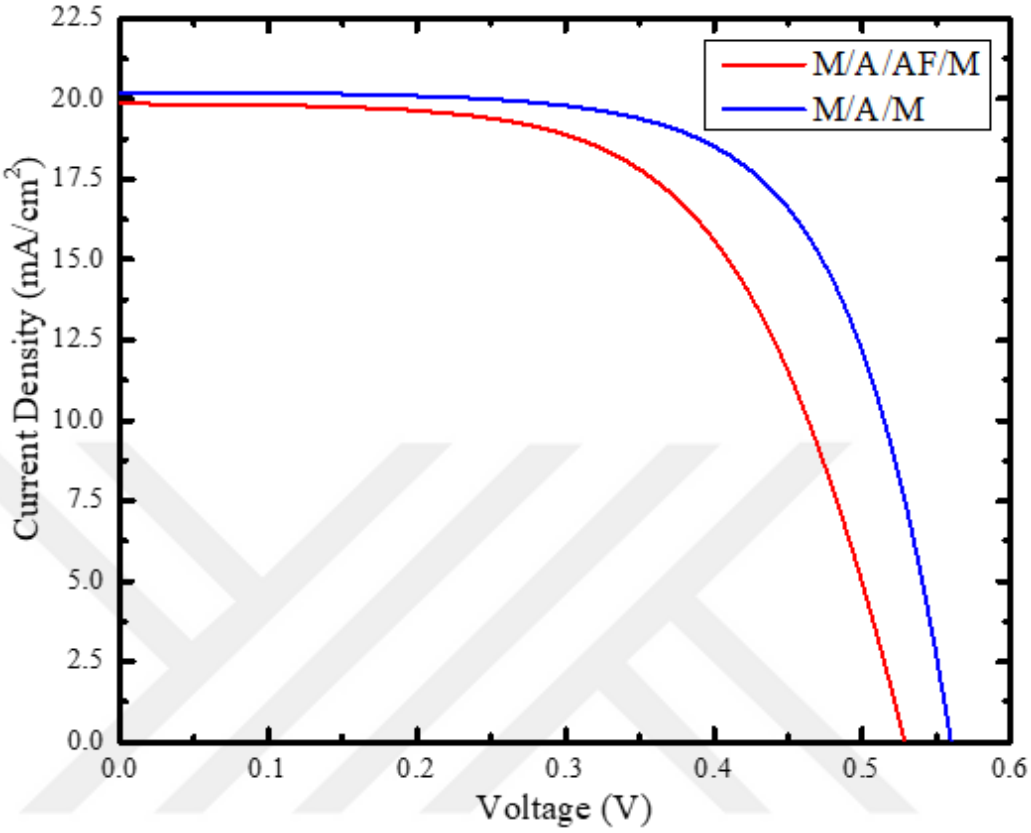

Figure 4.8 J-V curve comparison of solar cells employing M/A/M and M/A/AF/M HTTCE structure.

Measured current values are divided by the active area of the solar cells that they are measured from, to get the current density values for better comparison of solar cells utilizing M/A/M and M/A/AF/M HTTCEs. J-V curves of these solar cells are given in Figure 4.8, where it can be seen that the solar cell employing M/A/AF/M structure has lower V_{oc}, FF and J_{sc} values. Several solar cells are fabricated for both structures and the average V_{oc}, FF and J_{sc} values are 554.4 mV, 64.4% and 20.2 mA/cm^2 respectively for M/A/M, and 535.9 mV, 60.5% and 19.84 mA/cm^2 respectively for M/A/AF/M. Consequently the average efficiencies are 7.21% and 6.42% for solar cells employing M/A/M and M/A/AF/M structures respectively.

At first, it was expected to get better performance from M/A/AF/M structures, since the holes can be collected by the metal fingers directly after the Ag thin film without the necessity of passing through the outer MoO_x layer, such as in M/A/M structure. The small performance lost in M/A/AF/M compared to M/A/M strcuture seems to be caused by the fabrication process. M/A/M HTTCEs are deposited in situ in the vacuum chamber and the vacuum is broken only for the final process of applying the shadow mask for Ag metal finger deposition. On the other hand, in order to get M/A/AF/M structure, samples need to be unloaded from the thermal evaporation system by venting the vacuum chamber after the MoO_x/Ag layer depositions, to put a shadow mask for the deposition of Ag fingers. After that deposition, the samples again need to be taken out of the chamber before the last MoO_x layer deposition, to remove the first shadow mask and put the second one that protects the busbar from outer MoO_x layer deposition. It is possible that this process introduces contamination to the samples and application of shadow masks might be damaging the thin films, which could hinder the performance of the fabricated solar cells. More importantly, taking the samples out of vacuum environment and introducing them to air before the deposition of an outer MoO_x layer, most probably causes the oxidation of 10 nm Ag layer; thus, this seems to be the main reason for the failure of performance enhancement with M/A/AF/M design.

4.4. Optimization of Outer MoO_x Thickness

The thickness of layers in previous sections were fixed at 15nm/10nm/30nm for MoO_x/Ag/MoO_x. Outer MoO_x layer is used for enhancing the transmission of the HTTCE structure and protecting the Ag layer from oxidation. The thickness of this layer is varied between 30 – 60 nm to observe the effect of outer MoO_x thickness on electrical and optical properties of fabricated solar cells employing MoO_x/Ag/MoO_x HTTCE.

4.4.1. Electrical Characterization

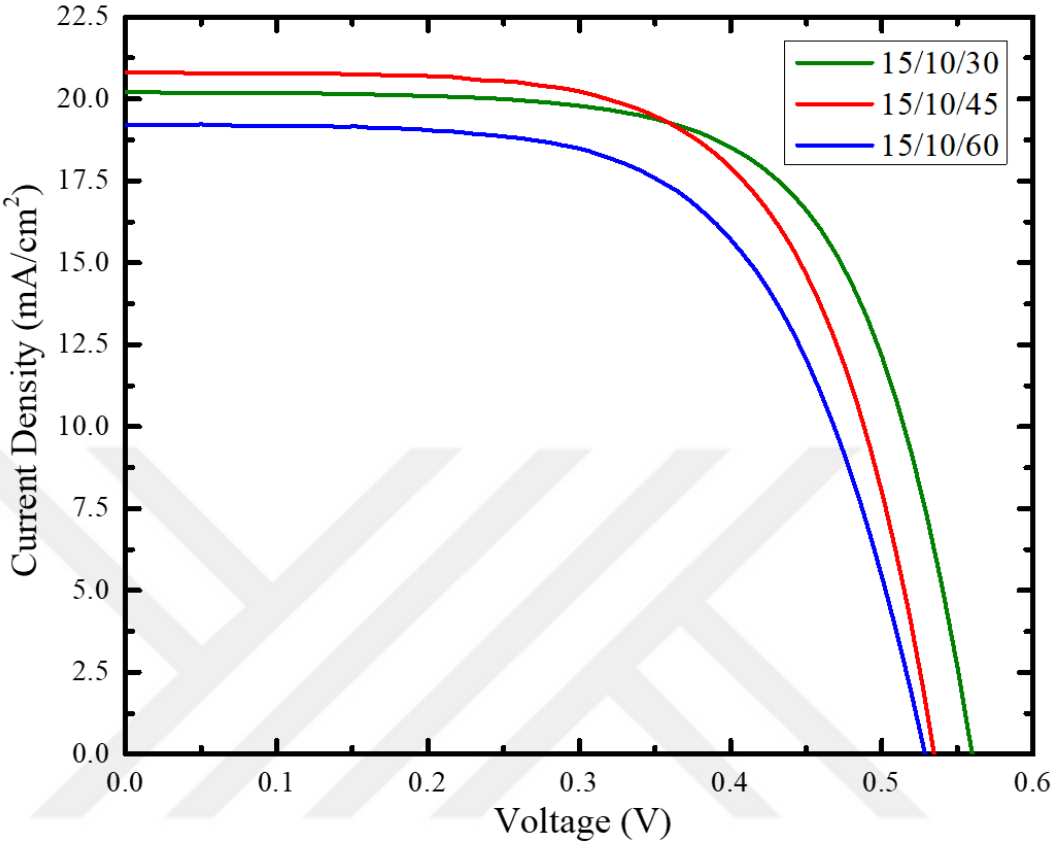

Figure 4.9 J-V curve comparison of solar cells employing M/A/M HTTCE with various outer MoOx thickness.

Example J-V curves of fabricated solar cells that utilizes HTTCE with different outer MoO_x layer thicknesses are given in Figure 4.9, and the average V_{oc}, J_{sc} and FF of the fabricated cells are given in Table 4.2. Variations in J_{sc} does not seem to show a trend and seems to be not very significant. However, V_{oc} and FF shows a decreasing trend with increasing outer MoO_x thickness. For FF, although the differences are not large, the decreasing trend was expected, as the increase in MoO_x layer is expected to increase the parasitic resistance, since the carriers need to be transported longer distances until they reach the front metal contact. Decrease in V_{oc} is better understood from the optical characterization; therefore, it is explained in section 4.4.2.

Table 4.2. *Average Voc, Jsc and FF values measured from solar cells employing HTTCE structures with different outer MoOx layer thicknesses*

$MoO_x/Ag/MoO_x$	V_{oc} *(mV)*	J_{sc} *(mA/cm²)*	*FF (%)*
15/10/30	554.4 ± 0.6	20.20 ± 0.1	64.39 ± 1.5
15/10/45	535.3 ± 1.8	20.82 ± 0.1	63.45 ± 0.5
15/10/60	526.9 ± 3.6	19.20 ± 0.2	62.07 ± 0.1

Average efficiencies of the cells are given in Figure 4.10, where it can be seen that efficiencies of fabricated solar cells also show a decreasing trend with increasing outer MoO_x layer thickness, which is as expected due to the decrease in V_{oc} and FF. Moreover, four point probe measurements revealed that R_{sheet} of these HTTCEs are between 7-7.5 Ω/sqr.

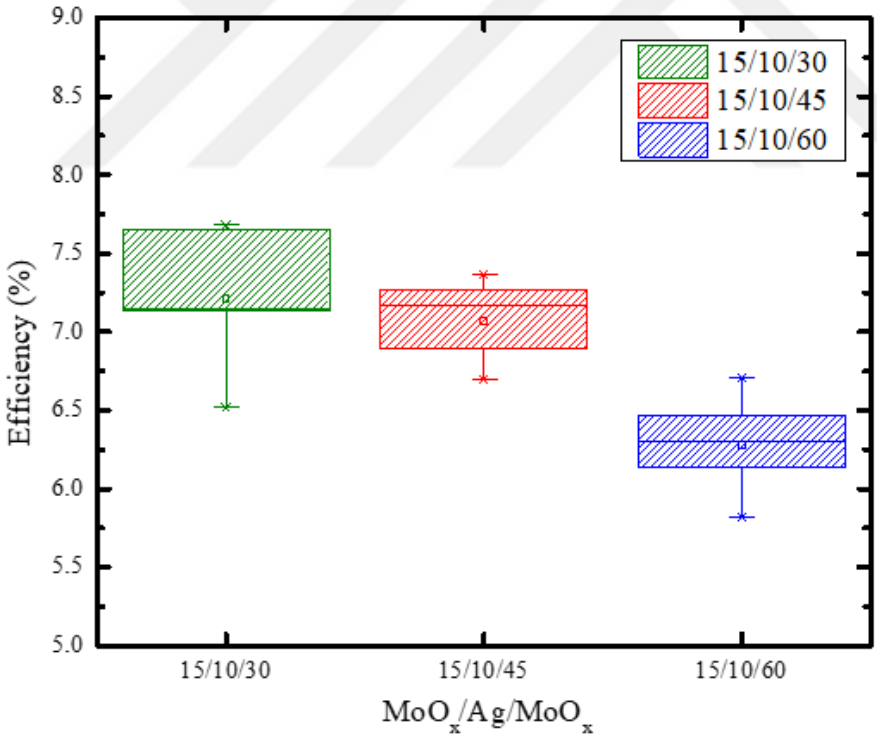

Figure 4.10 Efficiency comparison of solar cells employing M/A/M HTTCE structures with different outer MoOx thickness

4.4.2. Reflectance, Transmittance and Absorption

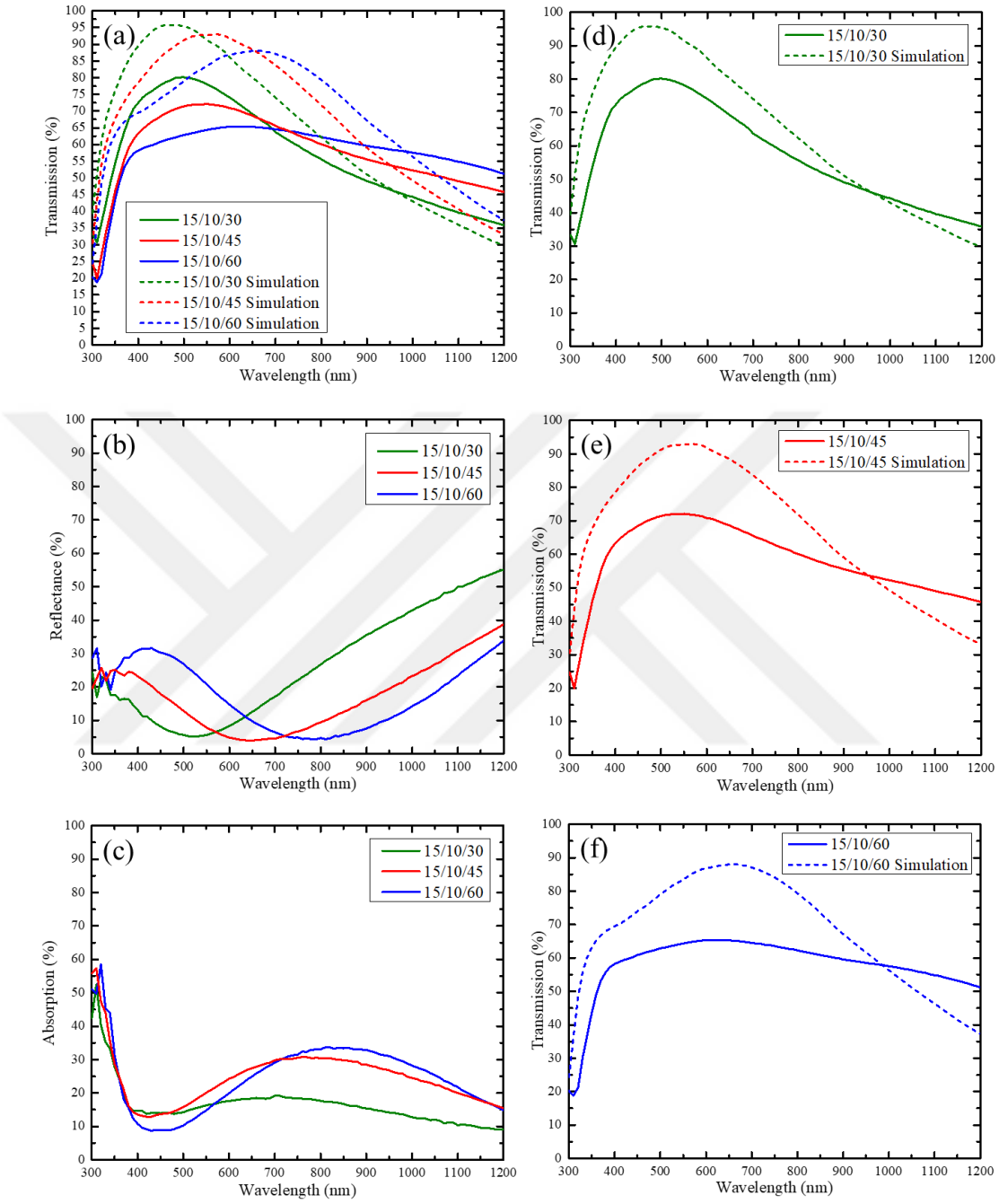

Figure 4.11 (a) Measured and simulated transmittance, (b) reflectance and (c) absorption comparisons of M/A/M HTTCE layers with different outer MoOx thicknesses, and separate transmittance plots including simulated transmittance of M/A/M with layer thicknesses of (d) 15nm/10nm/30nm, (e) 15nm/10nm/45nm and (f) 15nm/10nm/60nm

Figure 4.11(a) shows the measured and simulated transmittance of HTTCEs employing different outer MoO_x thicknesses. In addition to this, weighted transmission of HTTCEs with different outer MoO_x thicknesses are calculated by integration with AM 1.5 solar spectral irradiance, and given in Table 4.3 together with weighted reflection and absorption.

Table 4.3. *Weighted transmission, reflection and absorption of HTTCEs with different outer MoOx thicknesses*

MoO_x/Ag/MoO_x	*Weighted Transmission*	*Weighted Reflection*	*Weighted Absorption*
15/10/30	63.6%	20.2%	16.2%
15/10/45	62.9%	13.6%	23.5%
15/10/60	61%	16.5%	22.5%

It seems that as the thickness increases, the weighted transmission decreases. More importantly, it is observed from Figure 4.11(a) that as thickness increases, HTTCEs lose transmission in short wavelengths while gaining transmission in longer wavelengths. This seems to affect the V_{oc} of the fabricated solar cells, as V_{oc} of the solar cells seems to decrease with increasing outer MoO_x thickness. Shorter wavelengths are generally absorbed close to the front side of the solar cells while longer wavelengths are absorbed close to rear side. Since the junction of the fabricated solar cells are in MoO_x/c-Si interface, which is close to the front side, and since less carriers will be generated if the absorption in the junction is decreased; loss of transmission in shorter wavelengths could be the explanation of decrease in V_{oc} with increasing outer MoO_x thickness. Although the transmission increase in longer wavelengths are not as pronounced as the measured transmittance, simulated transmittance seems to follow a similar trend with the experimental findings. Figure 4.11(d), Figure 4.11(e) and Figure 4.11(f) is plotted for a clearer representation of simulated and measured transmittance of the HTTCE structures. Highest transmittance at 550 nm of 78% is achieved from HTTCE that has 15nm/10nm/30nm layer thicknesses. Although this transmittance is lower than the transmittance of

reported ITO (60 nm) TCE, which is 85% at that wavelength [Winkler et al., 2011], further optimizations on layer thicknesses could potentially lead to better optical properties.

Thin film interference effect is observed in Figure 4.11(b), where the response is shifted to longer wavelengths as thickness of outer MoO_x layer increases. Moreover, it can be seen from Figure 4.11(c) that absorption of longer wavelengths also increase with increasing outer MoO_x thickness, as the plasmon peaks show a red shift with increased outer MoO_x. This behaviour is expected, since the effective index of refraction in the surrounding area of Ag thin film is increasing simultaneously with outer MoO_x thickness [Cao et al., 2011].

4.4.3. Quantum Efficiency

EQE of the fabricated cells given in Figure 4.12(a) shows corellation with the reflectance of HTTCEs in Figure 4.11(b), as a shift towards higher wavelengths is observed. Reflectance of HTTCEs deposited on c-Si and IQE of fabricated solar cells are given in Figure 4.12(b), where the thin film interference effect on the reflectance is again observed. For the solar cell that has 60 nm outer MoO_x thickness (15/10/60), IQE seems to be as high as the IQE of the solar cell with 30 nm outer MoO_x thickness (15/10/30) in the wavelength range between 300 – 450 nm. This is due to the high reflection of 15/10/60 in that range which is caused by thin film interference effect. The drop in IQE of 15/10/60 after that wavelength range seems to be from high parasitic absorption at longer wavelengths.

Other than that, a general decrease of IQE is observed as the outer MoO_x thickness increases, due to simultaneous increase in parasitic absorption. The weighted absorptions given in Table 4.3does not show a directly proportional relation with increasing outer MoO_x thicknes; however, as discussed in section 4.2.1, those are relative absorption measurements to have an approximate idea of the optical properties, while the HTTCEs deposited on c-Si have different properties which are close to what is observed in the relative characterizations.

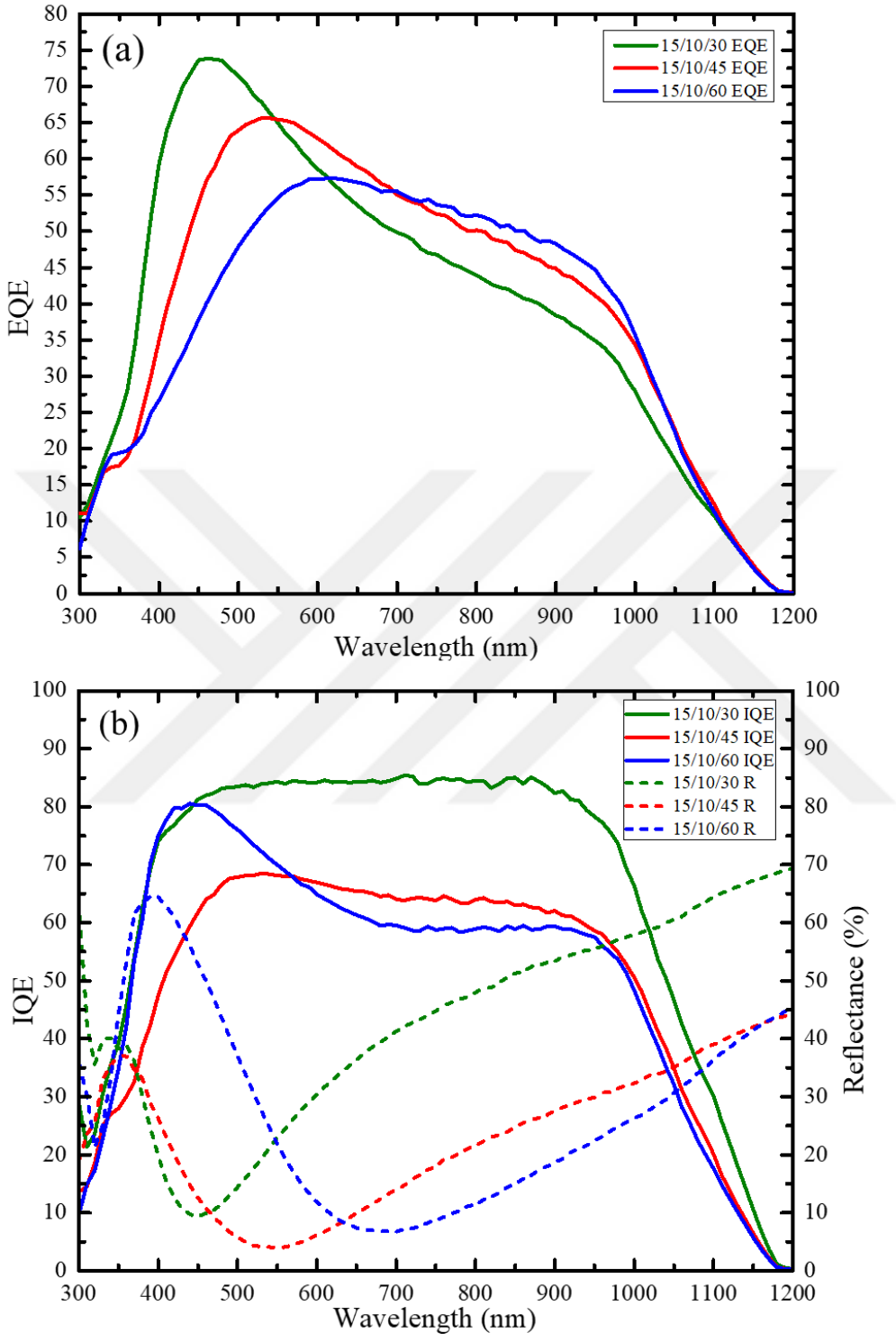

Figure 4.12 (a) EQE and (b) IQE comparisons of solar cells employing M/A/M HTTCE with different outer MoOx thicknesses. (b) also includes reflectance of HTTCE structures deposited on c-Si.

4.5. Textured c-Si substrate

HTTCEs with different outer MoO_x thicknesses are also deposited on front side pyramid textured c-Si, to enhance J_{sc} by light trapping caused by multiple reflections from pyramid structure on the surface.

4.5.1. Electrical Characterization

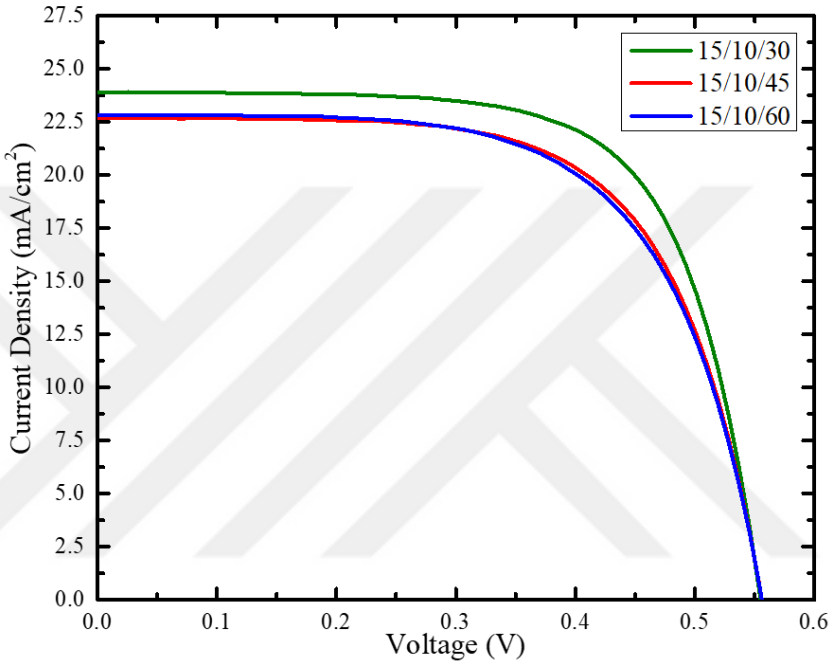

Figure 4.13 J-V curves of front side pyramid textured c-Si solar cells employing M/A/M HTTCE with various outer MoOx thickness.

Figure 4.13 shows the J-V curves of example front side pyramid textured c-Si solar cells with HTTCEs that utilize different outer MoO_x layer thicknesses and Table 4.4 gives the average V_{oc}, J_{sc} and FF values of those cells. Compared to the solar cells with flat surface, front side textured solar cells seems to have better J_{sc} values, which is probably enhanced by light trapping of pyramid textured surface.

The decrease in FF with increasing outer MoO_x thickness is again observed in the fabricated front side textured solar cells, due to increase in parasitic resistance. However, V_{oc} of the cells did not seem to decrease with increasing outer MoO_x thickness, as it decreased in flat surface solar cells which is discussed in section 4.4.2.

The absence of this effect may be caused by the enhancement of light transmission from the HTTCE due to the light trapping in pyramid textured surface, that enables some of the reflected light to interact with the surface multiple times. Hence, the V_{oc} of fabricated solar cells are close to each other, regardless of the thicknes of outer MoO_x layer. Therefore, FF seemed to be the deciding parameter for efficiency comparison, and the same decreasing trend in average efficiency with increasing outer MoO_x thickness which is observed previously in solar cells that has flat surface, is observed again in solar cells with textured surface, which can be seen in Figure 4.14. Enhancement in efficiencies are observed with front side textured solar cells compared to flat surface solar cells.

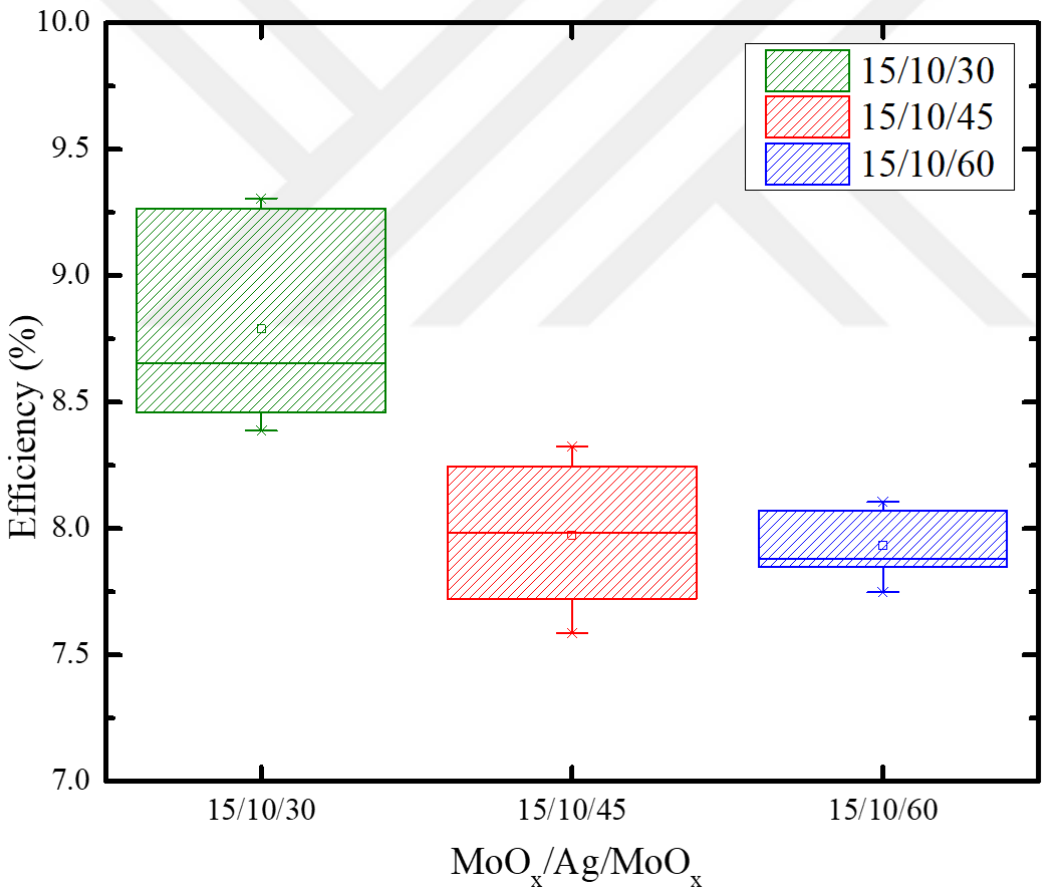

Figure 4.14 Efficiency comparison of front side pyramid textured solar cells that employ M/A/M HTTCE with different outer MoOx thicknesses.

Table 4.4. *Average Voc, Jsc and FF values of front side pyramid textured c-Si solar cells employing HTTCE structures with different outer MoOx layer thicknesses*

MoO_x/Ag/MoO_x	V_{oc} *(mV)*	J_{sc} *(mA/cm²)*	*FF (%)*
15/10/30	558.1 ± 2.6	23.8 ± 0.1	66.1 ± 0.8
15/10/45	561.2 ± 0.5	22.4 ±0.1	63.5 ± 1.1
15/10/60	554.2 ± 4.5	22.8 ± 0.1	62.8 ± 0.4

4.5.2. Quantum Efficiency

EQE and IQE of fabricated front side textured solar cells that employs HTTCEs with different outer MoO_x thicknesses are given in Figure 4.15(a) and Figure 4.15(b), respectively. Figure 4.15(b) also includes reflectance of HTTCEs deposited on textured c-Si.

From Figure 4.15(a) the shift to higher wavelengths with increasing outer MoO_x thickness can be seen again, as in Figure 4.12(a) for flat surface solar cells; although the shifts here are very small compared to the previous ones, due to broadband antireflection effect of the pyramid textured surface dominating the thin film interference effect.

From Figure 4.15(b), it is observed that solar cell employing HTTCE with 30 nm outer MoO_x thickness has the highest IQE. Hence, the decrease of IQE with increasing outer MoO_x thickness is again observed, although the difference of IQE between cells employing 45 nm and 60 nm outer MoO_x thickness is not too much. Moreover, front side textured solar cells seem to have lower IQE than flat surface cells. The multiple surface interactions of light caused by the pyramid structure also makes the light go through the HTTCE layer several times, where some of the parasitic absorptions occur. Thus, this could be enhancing parasitic absorption, which in turn, lowers IQE of fabricated solar cells.

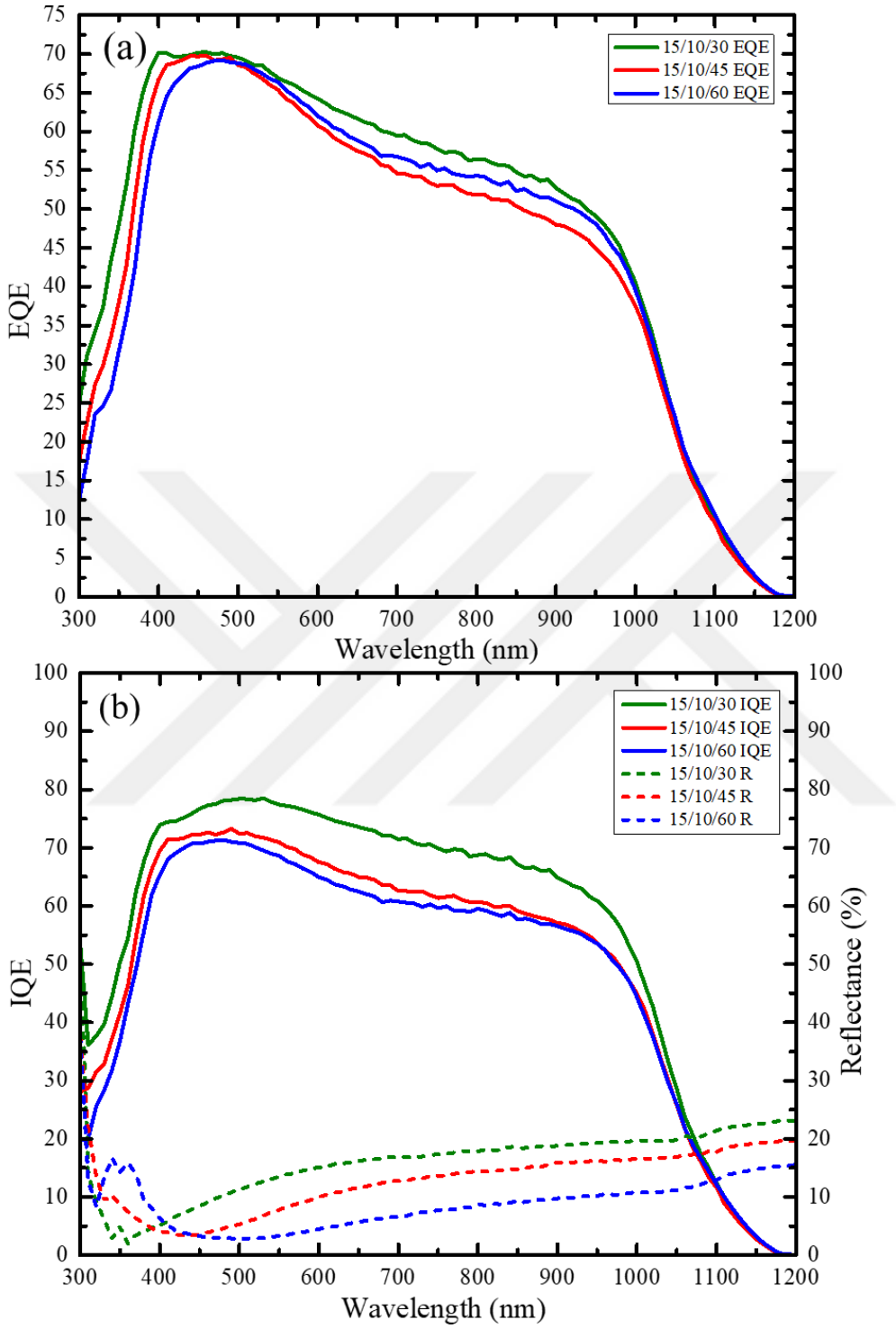

Figure 4.15 (a) EQE and (b) IQE comparisons of front side pyramid textured solar cells employing M/A/M HTTCE with different outer MoOx thicknesses. (b) also includes reflectance of HTTCE structures deposited on textured c-Si.

CHAPTER 5

CONCLUSIONS

In this study, HTTCE multilayers are developed to be used as alternatives to ITO and highly doped p+ layers in n-type c-Si solar cells. Several design optimizations to improve electrical and optical properties are performed and solar cell performances are compared.

Solar cells that employ identical MoO_x/Ag/MoO_x HTTCE structures, with 15 nm/10 nm/30 nm layer thicknesses, are fabricated from several different c-Si wafers and one of the wafers, given as wafer II in Table 3.1, is chosen to be used in the rest of this work, as the cells fabricated from that wafer showed better performance. Deposition rate of Ag thin film between two MoO_x layers is varied between 0.5 – 2.0 Å/s, and an increase in film uniformity with increasing rate is observed. However, high Ag deposition rate resulted in a decrease in V_{oc} of the fabricated solar cells, which suggests that a damage is induced during high rate Ag deposition, to the first 15nm MoO_x thin film which is in contact with c-Si. A mixed deposition rate of 1.0 Å/s for the first 5 nm and 1.5 Å/s for the remaining 5 nm of the 10 nm Ag film is also tried. Although HTTCEs fabricated with this mixed rate showed good optical properties, V_{oc} of the cells utilizing these structures were still low compared to lower rates. Therefore, 1.0 Å/s is chosen as the optimum deposition rate among the compared rates in this work.

As mentioned above, at 15 nm thick MoO_x thin film have shown to be a delicate material, such that deposition rate of Ag layer can affect the material properties. This behavior is further observed in a trial that a different HTTCE design is utilized, in which the metal fingers are incorporated without the 30 nm MoO_x cap layer. Fabrication process of solar cells utilizing this HTTCE design introduces

contamination, oxidation of Ag layer and possibly damage to the MoO_x/Ag multilayer that results in a 3.3% decrease in V_{oc} when compared with the solar cells that employ the metal fingers on top of the original HTTCE design. Problems in the fabrication process of this design caused decrease in performance, while an enhancement was expected. Hence, in situ shadow mask application or a thermal evaporation system in a glow box could be used for preventing the problems of the fabrication of solar cells with such HTTCE design, and possible enhancements in solar cell performance could be observed.

In above mentioned trials, layer thicknesses of MoO_x/Ag/MoO_x structures are fixed to 15 nm/10 nm/30 nm. Effect of outer MoO_x layer thickness is also investigated, as the thickness is varied between 30 – 60 nm. With the increasing outer MoO_x thickness, decrease in FF of the fabricated solar cells is observed due to increased resistance. In addition, as the outer MoO_x thickness increase, reduction of transmission in shorter wavelengths while increased transmission in longer wavelengths is observed. Simulated transmittance showed similar trends, although, transmission increase in longer wavelengths are not as pronounced as measured transmittance. Reduced transmission in shorter wavelengths consequently decreased the V_{oc} of the solar cells, since the carriers are generated closer to the front side of the fabricated solar cells in this work. The decrease and increase of transmission in shorter and longer wavelengths, respectively, is due to the shift in thin film interference effect to longer wavelengths caused by the change in the outer layer thickness of compared HTTCE multilayers.

Finally, HTTCEs with different outer MoO_x layer thicknesses are again compared for solar cells fabricated on pyramid textured n-type c-Si substrates. Decrease in FF as outer MoO_x thickness increased is again observed, however, V_{oc} did not change for these solar cells. This suggests that the increase in generated carriers due to multiple interactions of reflected light with the surface, compensates the loss in shorter wavelengths caused by the HTTCE layers with thicker outer MoO_x. Moreover, a general efficiency increase is observed in textured solar cells, compared to flat

surface solar cells, due to enhanced carrier generation caused by this light trapping. However, increase in parasitic absorption is also observed, which is due to light passing the HTTCE layer multiple times.

To conclude, an efficiency of 9.3 ± 0.2 % is achieved with a pyramid textured semi-dopant-free solar cell that employs MoO_x/Ag/MoO_x HTTCE structure with 15 nm/10 nm/30 nm layer thicknesses and no additional passivation interlayers between c-Si and selective contacts. Further improvements in this structure can be made by using a less resistive material than MoO_x, which also has less absorption, for the outer layer of the HTTCE and by incorporating a thin passivation layer between MoO_x and c-Si. The HTTCE structure presented in this thesis can be utilized in fabrication of full dopant-free solar cells in the future.

REFERENCES

Almora, O., Gerling, L. G., Voz, C., Alcubilla, R., Puigdollers, J., & Garcia-Belmonte, G. (2017). *Superior performance of V2O5 as hole selective contact over other transition metal oxides in silicon heterojunction solar cells*. Solar Energy Materials and Solar Cells, 168, pp. 221-226. doi:10.1016/j.solmat.2017.04.042

Battaglia, C., Nicolás, S. M., De Wolf, S., Yin, X., Zheng, M., Ballif, C., & Javey, A. (2014a). *Silicon heterojunction solar cell with passivated hole selective MoOx contact*. Applied Physics Letters, 104(11), 113902. doi:10.1063/1.4868880

Battaglia, C., Yin, X., Zheng, M., Sharp, I. D., Chen, T., McDonnell, S., Azcatl, A., Carraro, C., Ma, B., Maboudian, R., Wallace, R. M. & Javey, A. (2014b). *Hole Selective MoOx Contact for Silicon Solar Cells*. Nano Letters, 14(2), pp. 967-971. doi:10.1021/nl404389u

Bivour, M., Temmler, J., Steinkemper, H., & Hermle, M. (2015). *Molybdenum and tungsten oxide: High work function wide band gap contact materials for hole selective contacts of silicon solar cells*. Solar Energy Materials and Solar Cells, 142, pp. 34-41. doi:10.1016/j.solmat.2015.05.031

Blakers, A. W., Wang, A., Milne, A. M., Zhao, J., & Green, M. A., (1989*). 22.8% efficient silicon solar cell*. Applied Physics Letters, 55(13), pp. 1363-1365. doi:10.1063/1.101596

Bullock, J., Cuevas, A., Allen, T., & Battaglia, C. (2014). *Molybdenum oxide MoOx: A versatile hole contact for silicon solar cells*. Applied Physics Letters, 105(23), 232109. doi:10.1063/1.4903467

Bullock, J., Hettick, M., Geissbühler, J., Ong, A.J., Allen, T., Sutter-Fella, C.M., Chen, T., Ota, H., Schaler, E.W., De Wolf, S., Ballif, C., Cuevas, A. & Javey, A. (2016). *Efficient silicon solar cells with dopant-free asymmetric heterocontacts*. Nature Energy, 1, 15031. doi: 10.1038/nenergy.2015.31

Bullock, J., Wan, Y., Xu, Z., Essig, S., Hettick, M., Wang, H., Ji, W., Boccard, M., Cuevas, A., Ballif, C. & Javey, A. (2018). *Stable Dopant-Free Asymmetric Heterocontact Silicon Solar Cells with Efficiencies above 20%*. ACS Energy Letters, 3(3), pp. 508-513. doi:10.1021/acsenergylett.7b01279

Cao, J., Galbraith, E. K., Sun, T., & Grattan, K. T. (2011). *Comparison of Surface Plasmon Resonance and Localized Surface Plasmon Resonance-based optical fibre sensors*. Journal of Physics: Conference Series, 307, 012050. doi:10.1088/1742-6596/307/1/012050

Cattin, L., Lare, Y., Makha, M., Fleury, M., Chandezon, F., Abachi, T., Morsli, M., Napo, K., Addou, M. & Bernéde, J.C. (2013) *Effect of the Ag deposition rate*

on the properties of conductive transparent MoO3/Ag/MoO3 multilayers. Solar Energy Materials & Solar Cells, 117, pp. 103 – 109. doi:10.1016/j.solmat.2013.05.026

De Wolf, S., Descoeudres, A., Holman, Z. C., & Ballif, C. (2012). *High-efficiency Silicon Heterojunction Solar Cells: A Review*. Green, 2(1), pp. 7-24. doi:10.1515/green-2011-0018

Ellmer, K. (2012). *Past achievements and future challenges in the development of optically transparent electrodes*. Nature Photonics, 6(12), 809-817. doi:10.1038/nphoton.2012.282

Feldmann, F., Simon, M., Bivour, M., Reichel, C., Hermle, M., & Glunz, S. W. (2014). *Carrier-selective contacts for Si solar cells*. Applied Physics Letters, 104(18), 181105. doi:10.1063/1.4875904

Fraunhofer Institute for Solar Energy Systems, ISE. (2018). *©Fraunhofer ISE: Photovoltaics Report, updated: 27 August 2018*, Retrieved from: https://www.ise.fraunhofer.de

Gerling, L. G., Mahato, S., Morales-Vilches, A., Masmitja, G., Ortega, P., Voz, C., Alcubilla, R. & Puigdollers, J. (2016). *Transition metal oxides as hole-selective contacts in silicon heterojunctions solar cells*. Solar Energy Materials and Solar Cells, 145, pp. 109-115. doi:10.1016/j.solmat.2015.08.028

Glunz, S.W., Preu, R. & Biro, D. (2012). *Crystalline Silicon Solar Cells: State-of-the-Art and Future Developments*. In A. Sayigh (Ed.), Comprehensive Renewable Energy. pp. 353-387, Elsevier Ltd. doi:10.1016/B978-0-08-087872-0.00117-7

Goetzberger, A., Hebling, C., & Schock, H. (2003). *Photovoltaic materials, history, status and outlook*. Materials Science and Engineering: R: Reports, 40(1), pp. 1-46. doi:10.1016/s0927-796x(02)00092-x

Greiner, M. T., Chai, L., Helander, M. G., Tang, W., & Lu, Z. (2012). *Transition Metal Oxide Work Functions: The Influence of Cation Oxidation State and Oxygen Vacancies*. Advanced Functional Materials, 22(21), pp. 4557-4568. doi:10.1002/adfm.201200615

Guo, X., Liu, X., Lin, F., Li, H., Fan, Y., & Zhang, N. (2015). *Highly Conductive Transparent Organic Electrodes with Multilayer Structures for Rigid and Flexible Optoelectronics*. Scientific Reports, 5(1). doi:10.1038/srep10569

Han, H., Theodore, N. D., & Alford, T. L. (2008). *Improved conductivity and mechanism of carrier transport in zinc oxide with embedded silver layer*. Journal of Applied Physics, 103(1), 013708. doi:10.1063/1.2829788

ITRPV, (2018). *International Technology Roadmap for Photovoltaic Results 2017 including maturity report 2018 (Ninth Edition).* Retrieved from http://www.itrpv.net

Kim, N., Um, H., Choi, I., Kim, K. & Seo, K. (2016). *18.4%-Efficient Heterojunction Si Solar Cells Using Optimized ITO/Top Electrode.* Applied Materials & Interfaces. 8, pp.11412-11417, doi: 10.1021/acsami.6b00981

Kittel, C., & McEuen, P., (2005). *Introduction to solid state physics* (8th ed.). John Wiley & Sons.

Klein, A., Körber, C., Wachau, A., Säuberlich, F., Gassenbauer, Y., Harvey, S.P., Proffit, D.E. & Mason, T. O. (2010). *Transparent Conducting Oxides for Photovoltaics: Manipulation of Fermi Level, Work Function and Energy Band Alignment*. Materials, 3(11), pp. 4892-4914. doi:10.3390/ma3114892

Mandelkorn, J., & Lamneck, J. H. (1990). Simplified fabrication of back surface electric field silicon cells and novel characteristics of such cells. Solar Cells, 29(2-3), pp. 121-130. doi:10.1016/0379-6787(90)90021-v

Melskens, J., Van De Loo, B. W., Macco, B., Black, L. E., Smit, S., & Kessels, W. M. (2018). Passivating Contacts for Crystalline Silicon Solar Cells: From Concepts and Materials to Prospects. IEEE Journal of Photovoltaics, 8(2), pp. 373-388. doi:10.1109/jphotov.2018.2797106

Minami, T. (2005). Transparent conducting oxide semiconductors for transparent electrodes. Semiconductor Science and Technology, 20(4), doi:10.1088/0268-1242/20/4/004

Morales-Masis, M., De Wolf, S., Woods-Robinson, R., Ager, J.W. & Ballif, C. (2017). *Transparent Electrodes for Efficient Optoelectronics*. Advanced Electronic Materials, 3(5), 1600529, doi:10.1002/aelm.201600529

Müller, J., Rech, B., Springer, J. & Vanecek, M. (2004). *TCO and light trapping in silicon thin film solar cells*. Solar Energy, 77(6), pp.917-930, doi:10.1016/j.solener.2004.03.015

Nasser, H., Kökbudak, G., Mehmood, H., & Turan, R. (2017). *Dependence of n-cSi/MoOx Heterojunction Performance on cSi Doping Concentration*. Energy Procedia, 124, pp. 418-424. doi:10.1016/j.egypro.2017.09.267

Nemeth, B., Young, D. L., Page, M. R., Lasalvia, V., Johnston, S., Reedy, R., & Stradins, P. (2016). *Polycrystalline silicon passivated tunneling contacts for high efficiency silicon solar cells*. Journal of Materials Research, 31(06), pp. 671-681. doi:10.1557/jmr.2016.77

Ng, K. K., & Card, H. C. (1980). *Asymmetry in the SiO2 tunneling barriers to electrons and holes*. Journal of Applied Physics, 51(4), 2153. doi:10.1063/1.327888

Nguyen, D.-T., Vedraine, S., Cattin, L., Torchio, P., Morsli, M., Flory, F. & Bernéde, J. C. (2012). *Effect of the thickness of the MoO3 layers on optical properties of MoO3/Ag/MoO3 multilayer structures*. Journal of Applied Physics, 112(6), pp. 063505. doi:10.1063/1.4751334

Ohl, R. S. (1941). *U.S. Patent No. US240252*

Omnes, F., (2010). *Introduction to Semiconductor Photodetectors*. In D. Decoster & J. Harari (Eds.), *Optoelectronic Sensors.* pp.1-14, London, John Wiley & Sons.

Pedrotti, F. L., & Pedrotti, L. S. (1992). *Introduction to optics* (2nd ed.). Prentice Hall.

Quimby, R. S., (2006). *Photonics and Lasers: An Introduction*. John Wiley & Sons.

Sharma, V., Kumar, P., Kumar, A., Surbhi, Asokan, K., & Sachdev, K. (2017). *High-performance radiation stable ZnO/Ag/ZnO multilayer transparent conductive electrode*. Solar Energy Materials and Solar Cells, 169, 122-131. doi:10.1016/j.solmat.2017.05.009

Shen, L., Xu, Y., Meng, F., Li, F., Ruan, S., & Chen, W. (2011). *Semitransparent polymer solar cells using V2O5/Ag/V2O5 as transparent anodes*. Organic Electronics, 12(7), pp. 1223-1226. doi:10.1016/j.orgel.2011.03.036

Shockley, W., & Queisser, H. J. (1961). *Detailed Balance Limit of Efficiency of p-n Junction Solar Cells*. Journal of Applied Physics, 32(3), pp. 510-519. doi:10.1063/1.1736034

Um, H., Kim, N., Lee, K., Hwang, I., Seo, J. H., & Seo, K. (2016). *Dopant-Free All-Back-Contact Si Nanohole Solar Cells Using MoOx and LiF Films*. Nano Letters, 16(2), pp. 981-987. doi:10.1021/acs.nanolett.5b03955

Wang, A., Zhao, J., & Green, M. A., (1990). *24% efficient silicon solar cells*. Applied Physics Letters, 57(6), pp. 602-604. doi:10.1063/1.103610

Winkler, T., Schmidt, H., Flügge, H., Nikolayzik, F., Baumann, I., Schmale, S., Weimann, T., Hinze, P., Johannes, H., Rabe, T., Hamwi, S., Riedl, T., Kowalsky, W. (2011). *Efficient large area semitransparent organic solar cells based on highly transparent and conductive ZTO/Ag/ZTO multilayer top electrodes*. Organic Electronics, 12(10), pp. 1612-1618. doi:10.1016/j.orgel.2011.06.015

Wu, C., Chen, P. S., Peng, C., & Wang, C. (2013). *TiOx/Ag/TiOx multilayer for application as a transparent conductive electrode and heat mirror*. Journal of Materials Science: Materials in Electronics,24(7), 2461-2468. doi:10.1007/s10854-013-1118-1

Wu, W., Bao, J. Liu, Z., Lin, W., Yu, X., Cai, L., Liu, B., Song, J. & Shen, H. (2016a). *MultilayerMoOx/Ag/MoOx emitters in dopant-free silicon solar cells.* 189, pp. 86-88. doi:10.1016/j.matlet.2016.11.059

Wu, W., Bao, J., Jia, X., Liu, Z., Cai, L., Liu, B., Song, J. & Shen, H. (2016b). *Dopant-free back contact silicon heterojunction solar cells employing transition metal oxide emitters*. Physica Status Solidi (RRL) - Rapid Research Letters,10(9), pp. 662-667. doi:10.1002/pssr.201600254

Zienkiewicz, O. C., Taylor, R. L., & Zhu, J. Z. (2013). *The finite element method: Its basis and fundamentals*. Amsterdam: Elsevier, Butterworth-Heinemann.